



universität
wien

MASTERARBEIT

Titel der Masterarbeit

„Spectroscopic Mode Identification of
the δ Scuti Star 4 CVn“

Verfasserin

Valentina Schmid, Bakk. rer. nat.

angestrebter akademischer Grad

Master of Science (MSc)

Wien, 2012

Studienkennzahl lt. Studienblatt:

A 066 861

Studienrichtung lt. Studienblatt:

Masterstudium Astronomie UG2002

Betreuerin / Betreuer:

emer. o. Univ.-Prof. Dr. Michel Breger

Zusammenfassung

Das Gebiet der Asteroseismologie beschäftigt sich vornehmlich mit der Theorie stellarer Pulsationen. Da die Eigenschaften der Schwingungen stark von der Struktur und dem Aufbau der Sterne abhängen, kann durch ihre Untersuchung ein einmaliger Blick ins Sterninnere geworfen werden. Die dadurch gewonnenen Erkenntnisse können dazu beitragen unser Verständnis der physikalischen Abläufe, der Entwicklung und der Zusammensetzung dieser Himmelskörper zu verbessern.

In der vorliegenden Arbeit wird der δ Scuti-Stern 4 CVn untersucht. Es handelt sich hierbei um einen Stern, von dem schon seit einigen Jahrzehnten spektroskopische und photometrische Daten gesammelt worden sind, und der bereits in zahlreichen Publikationen eingehend untersucht worden ist (Breger et al., 1999; Breger, 2000b; Breger et al., 2008; Breger, 2010). In der vorliegenden Arbeit wurden Daten, die über einen Zeitraum von vier Monaten am 2.1 m Otto-Struve-Teleskop des McDonald Observatorium in den Davis Mountains in West Texas, USA gewonnen worden sind, mit Hilfe des Computerprogramms IRAF reduziert und für weitere Untersuchungen aufbereitet. Ein starker Trend in der Radialgeschwindigkeitskurve deutet darauf hin, dass 4 CVn Teil eines Doppelsternsystems mit einer Periode der exzentrischen Bahn von 124,3 Tagen ist.

Anschließend wurde das zeitlich variierende Profil einer Absorptionslinie untersucht. Durch eine Fourieranalyse konnten elf Frequenzen, von denen acht bereits photometrisch nachgewiesen worden sind, entdeckt werden. Für diese elf Moden wurde anschließend eine Modenidentifikation durchgeführt. Es konnte jeder Pulsation Werte für die Quantenzahlen (ℓ, m) zugewiesen werden, wobei die drei nur in den spektroskopischen Datenstzen nachgewiesenen Frequenzen hohe ℓ -Werte größer als 4 haben.

Im Folgenden werde ich mich eingehend mit den verwendeten Methoden befassen und jede einzelne ausführlich erklären. Ich werde die Ergebnisse meiner Analyse präsentieren und diese in bezug zu einer bereits publizierten spektroskopischen Studie über 4 CVn (Castanheira et al., 2008) stellen.

Abstract

The study of stellar pulsations is one of the main components of asteroseismology. Since stellar oscillations largely depend on the stellar interior, the frequency, amplitude, and geometry of the modes provide a unique view into the inside of a star. Thus, the investigation of pulsational properties reveals important information on the internal stellar structure, which is used to improve stellar models.

This thesis deals with the analysis of spectroscopic measurements of the δ Scuti star 4 CVn, which is a well studied pulsator (Breger et al., 1999; Breger, 2000b; Breger et al., 2008; Breger, 2010). The star was observed for four months with the 2.1 m Otto-Struve telescope at McDonald Observatory, which is located in the Davis Mountains in West Texas, USA, using the Sandiford Cassegrain Echelle spectrograph. The obtained data were reduced with the help of the software tool IRAF, preparing them for further interpretation regarding their time-dependent properties.

The reduction process revealed a strong non-sinusoidal periodicity in the first moment of the line profile, which is usually related to radial velocity. This trend was discovered to be due to binary motion. A Keplerian orbit of high eccentricity and a period of 124.3 d was fitted to the data and subsequently subtracted to correct the radial velocity shift.

A following frequency analysis resulted in the detection of eleven frequencies, of which eight were already found in photometric data sets. By means of the Fourier parameter fit method, which interprets the profile variations of the absorption lines, a mode identification was carried out. Values of (ℓ, m) could be assigned to all the eleven modes. The three frequencies which were only detected in spectroscopic data sets turned out to be high-degree modes with $\ell > 4$.

In the present thesis, I will discuss the applied methods in detail. I will present the obtained results and discuss them with regard to a previously published spectroscopic study (Castanheira et al., 2008).

Contents

Zusammenfassung	iii
Abstract	iv
1 Introduction	1
1.1 Geometry of the pulsations	3
1.1.1 Radial modes	3
1.1.2 Non-radial modes	4
1.1.3 Stellar rotation	5
1.1.4 Pressure and gravity modes	6
1.2 The κ mechanism	7
1.3 δ Scuti stars in general	8
1.4 4 CVn so far	9
2 Observations and Data Reduction	16
2.1 Observations	16
2.2 Data Reduction	18
2.3 Binary motion	21
3 Methods	24
3.1 Frequency analysis	24
3.1.1 The Fourier transform	25
3.1.1.1 The spectral window and aliasing	29
3.1.2 Least-squares fit	33
3.1.2.1 Mono-periodic signals	33
3.1.2.2 Multi-periodic pulsations	35
3.1.3 The significance of the frequencies	35
3.2 Mode identification	36
3.2.1 Line-profile variations	37

CONTENTS

3.2.1.1	Selection of lines	39
3.2.2	The moments of the line	40
3.2.2.1	Frequency analysis and mode identification with the moments	41
3.2.3	The Fourier parameter fit method	42
3.2.3.1	Chi-square test	43
3.2.3.2	Genetic optimization algorithm	45
4	Results	47
4.1	The absorption lines	47
4.2	Frequency analysis	47
4.3	Mode identification	51
5	Conclusion	61
	Bibliography	64
	Danksagung	67
	Curriculum Vitae	69

Chapter 1

Introduction

Stars are anything but quiet objects floating through the night sky. From the lowest mass stars at the lower end of the main sequence to the largest giants, stars pulsate in many different manners throughout their whole life. Starting at a very young age, even before they reach the *zero-age main sequence* (ZAMS) and thermal equilibrium, they already exhibit pulsations, while they cross the *classical instability strip*. This is a special region in the pulsation Hertzsprung-Russell Diagram (HR Diagram), where more pulsating stars can be detected than anywhere else. Figure 1.1 depicts such an HR Diagram and the many different classes of pulsating stars. The classical instability strip is indicated by the two horizontal lines on the right-hand side.

After the hydrogen core burning has been initiated, stars leave the pre-main sequence stage and enter the longest phase of their lives, many of them pulsating. Depending on their mass, the oscillations will vary in terms of frequency, amplitude, geometry and excitation mechanism leading to solar-like oscillations, γ Dor and δ Sct pulsators or slowly pulsating B stars, among many others. As soon as hydrogen is depleted in the core, stars enter the most tumultuous phase of their lives as red giants. They pulsate as RR Lyrae stars or Cepheids while crossing the instability strip again before they end as old pulsating White Dwarfs.

Aerts et al. (2010) gave a detailed discussion about the many different classes of pulsating stars including illustrative examples.

The reason why pulsating stars are so interesting and why they are studied in such great detail, is that their oscillations provide us with a unique view into their interiors. Pressure or gravity waves that travel through the star give rise to distortions on the surface, periodical swelling and contracting and thus will change the light radiated. It are these periodic light variations that we can observe and

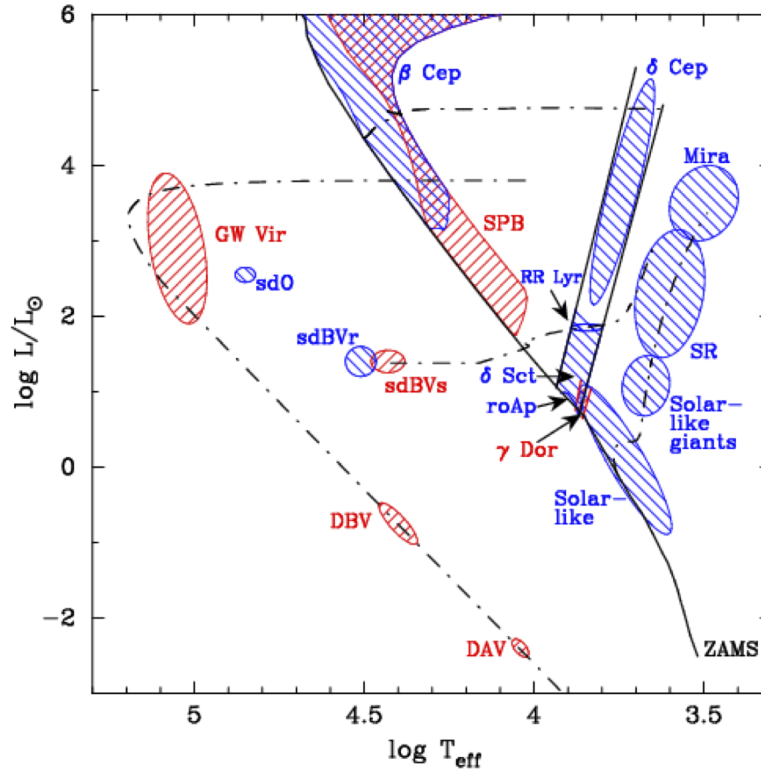


Figure 1.1: A Hertzsprung-Russell Diagram showing the different classes of pulsating stars as seen in Aerts et al. (2010). Red areas represent stars with g-mode oscillations and blue areas mark stars that pulsate with p-modes. Indicated by the two horizontal lines on the right side of the diagram is the classical instability strip.

interpret towards frequency, amplitude and phase of the oscillations.

A pressure wave is a propagating compression of gas, which moves at the speed of sound. For the simplified approximation of the star as an adiabatic system, the speed of sound can be written as $c = \sqrt{\gamma p / \rho}$, where γ denotes the adiabatic index, p is the pressure and ρ is the density of the gas. Assuming an ideal gas, the equation of state is $p = \rho k_B T / m_M$, with k_B being the Boltzmann constant and m_M being the molecular mass. Hence, the speed of sound is not only sensitive to pressure and density, but also to temperature and chemical composition. By applying basic physics, we can derive the speed of sound from the observed oscillations and thus get a good picture about the prevailing conditions inside a star.

However, a star is not uniform in its temperature profile and chemical composition, i.e., the fractions of the elements change throughout the interior. This causes a variation in density and pressure and, consequently, of the sound speed. Different oscillations will penetrate to different depths of the star, as they are reflected at

layers with a steep density gradient, which is also the reason why the waves are “trapped” inside the star. Accordingly, multi-periodic stars allow for a mapping of the density gradient in the cross-section of stars.

In the following sections I will discuss the geometry of the mode, i.e., radial and non-radial pulsations, the difference between p-modes and g-modes and their excitation mechanisms (following the explanations by Aerts et al. (2010)). I will give an overview of the class of δ Scuti stars and give details on the findings about the star 4 Canum Venaticorum, which is the main subject of this thesis. In Chapter 2 I will describe the observations and data that I used for my analysis. Chapter 3 provides an outline of the applied methods and in Chapter 4 I will present the results. A discussion and conclusion about the matter will be given in the Chapter 5, the last chapter.

1.1 Geometry of the pulsations

An oscillating one-dimensional string (for example, the string of a guitar or any other musical instrument) has nodal points in one direction only. These are points on the string that do not move with respect to the other parts of the string. Being a three-dimensional object with the spherical coordinates (r, θ, ϕ) , a star may oscillate with nodal points in three directions, one for each coordinate. They are represented by the three quantum numbers (n, ℓ, m) . An elaborate description of the displacements in the three-dimensional star and the geometry of the pulsations can be found in Aerts et al. (2010) or Collins (1989, chapter 8).

1.1.1 Radial modes

In the simplest case, the star keeps its spherical symmetry and only expands and contracts in the direction of the radius r . A uniform oscillation without any nodal points, where $n = 0$, is called the *fundamental radial mode*. The *first overtone* has one node, $n = 1$, which is a concentric shell within the star that does not move, similar to the nodal point of the one-dimensional string. Above and below this shell, the movements of the displacements occur in opposite directions. The second overtone then has two nodes with $n = 2$ and so forth.

For a guitar string, which has a homogeneous composition, the ratios of the periods of the fundamental mode to the first overtone is a small integer value,

therefore they are harmonic. However, this is not the case in stars that pulsate in the $n = 0$ and $n = 1$ radial mode simultaneously, i.e., the overtones are not harmonics of the fundamental mode. Thus, we can assume that temperature and chemical composition are not uniform throughout those stars (Aerts et al., 2010).

This basic assumption already shows that asteroseismology provides very powerful instruments to understand the interior mechanisms of a star. The more complex the oscillations become the more comprehensive and deeper our view into the stars will get.

1.1.2 Non-radial modes

Pulsations that also displace the stellar surface in such a way that certain regions are moving in opposite directions, are called *non-radial modes*. Contracting surface elements are thereby always situated next to swelling parts and vice versa, only separated by a stationary nodal line. We assume that the axis of symmetry for the pulsations is equal to the rotational axis, which is true for most pulsating stars. The nodes can be directed in either co-latitude θ , which is a measure for the polar angle, or longitude ϕ . The degree ℓ defines the total number of surface nodes, while the absolute value of the azimuthal order $|m|$ is the number of lines along a meridian, with $-\ell \leq m \leq +\ell$. It follows that there are $2\ell + 1$ possible values for m .

The non-radial mode with the lowest possible degree ($\ell = 1$) is called a *dipole* mode. It can either be *axisymmetric*, meaning that there are no meridian nodal lines ($m = 0$), or *sectoral*, where $\ell = |m|$. A mode of the next higher degree ($\ell = 2$) is called *quadrupole*, while an *octupole* mode already has three surface node lines. Whenever $|m| > 0$ and $m \neq \ell$ one speaks of a *tesseral* mode. Figure 1.2 depicts Doppler maps of stellar surfaces with an octupole mode at an inclination angle of $i = 45^\circ$ and with different orders.

In practice we are only able to measure the total brightness or Doppler velocity integrated over the stellar surface. Since adjacent regions will always have opposite signs in intensity and radial velocity, it is apparent that the values will average out in such integrated measurements. This effect, which is called *partial cancellation*, is more pronounced the higher the degree of the mode and especially for odd values of ℓ . The detection of modes in photometric light curves is thus limited to degrees $\ell < 4$ (Aerts et al., 2010). Spectroscopic line-profile variations, on the other hand, are less prone to partial cancellation effects, since they do not represent an integrated value.

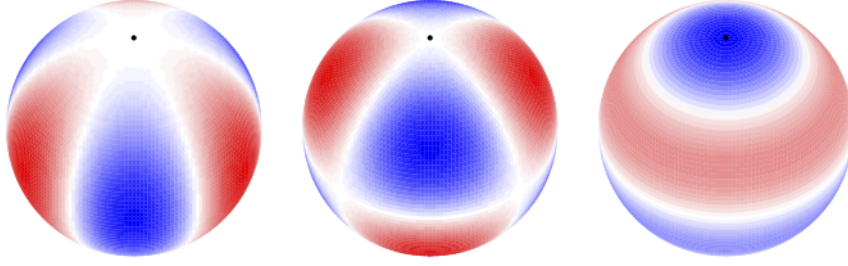


Figure 1.2: Surface velocity maps of a star pulsating in the octupole mode ($\ell = 3$) at an inclination angle of $i = 45^\circ$, as seen in Aerts et al. (2010). Red areas are surface elements moving away from the observer, while blue parts represent movements towards the observer, the white lines in between are the nodal lines and the black dots mark the north pole of the star. From left to right we see: pulsation in the sectoral mode $(\ell, m) = (3, 3)$, the tesseral mode $(\ell, m) = (3, 2)$ and the axisymmetric or zonal mode $(\ell, m) = (3, 0)$.

In fact, modes up to $\ell = 13$ have already been confirmed by means of spectroscopic mode identification (Zima, 2005).

1.1.3 Stellar rotation

Waves with a nodal line in the direction of longitude ($m \neq 0$) are traveling around the star. Depending on the sign of the temporal dependence $\exp(-i2\pi\nu t)$ of the spherical harmonics $Y_\ell^m(\theta, \phi)$ (for a definition see Aerts et al. (2010)), the direction of the propagation of the sectoral waves changes. In the case of a negative exponent, as shown in the above example, positive values of m represent movement in the same direction of rotation, thus they are called *prograde* modes. Accordingly, modes with negative m values move against the direction of rotation and are called *retrograde* modes. I adopted this convention for the present thesis.

If we assume a non-rotating star, the frequencies of the modes for all possible combinations of (ℓ, m) will be the same. Whenever rotation is present, the Coriolis force combined with other effects and the additional rotational frequency result in an increase in frequency for prograde modes and a decrease in frequency for retrograde modes. This will lead to an effect known as *rotational splitting*, where all $2\ell + 1$ different modes are equally spaced in the frequency spectrum. However, in practice not all modes are excited to such an extent that their amplitudes are detectable. In other words, a rotationally split multiplet might not always be recognizable as such.

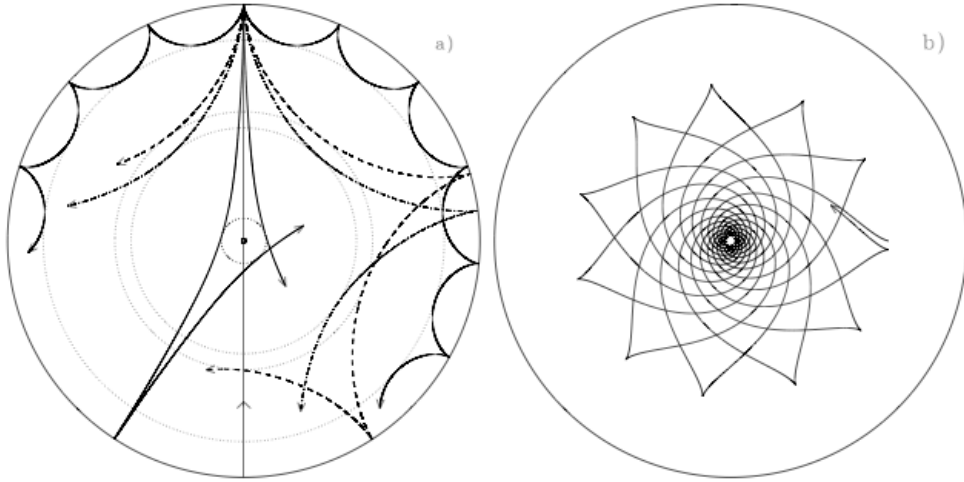


Figure 1.3: Ray paths of p-modes and g-modes in a cross-section of a Sun-like star. Panel a) shows the propagation of acoustic rays, as they are bent by increasing sound speed until they are totally refracted. The steep density gradient at the surface reflects the acoustic waves back into the interior of the star. The gravity waves, depicted in panel b), are reflected by the convective layers. From Cunha et al. (2007).

1.1.4 Pressure and gravity modes

There are two different types of waves that occur in stellar pulsation: *p-modes* and *g-modes*. The above mentioned p-modes are pressure or acoustic waves, where pressure acts as a restoring force. Since they mainly oscillate in the direction of propagation, they are longitudinal waves. The g-modes, or gravity modes, are transverse waves, meaning that the gas motions are perpendicular to the direction of propagation. Their main restoring force is buoyancy.

In general, p-modes have higher frequencies with increasing overtone n and degree ℓ , while the frequencies of g-modes are decreasing for a higher number of nodal lines. Furthermore, the amplitudes of p-modes are higher in the outer regions of the star. For g-modes, the opposite is true: their amplitudes are larger in the central regions, although they are still detectable on the surface of some stars, like γ Dor pulsators. Thus, they help to determine the limiting parameters of the physics of stellar cores.

For a better understanding, we can view the waves as propagating rays (see Figure 1.3). Whenever a non-radial p-mode penetrates to deeper layers of the star it is reflected by the higher sound speed prevailing in regions of higher density and temperature. At the surface the mode again encounters a change in those quantities

and is therefore directed back into the star. Hence, an acoustic wave cannot leave the stellar interior. The higher the degree of the mode, the smaller is the depth into which the ray penetrates and the more often it is reflected on the surface (although this number is not equal to ℓ).

Similarly, the ray paths of g-modes are constrained by convective regions. For low-mass stars, convection takes place in the outer parts. Consequently, gravity waves in the interior are reflected by this layer. In high-mass stars with convective cores, the rays of g-modes only propagate in the radiative envelope.

1.2 The κ mechanism

Stars are usually in a state of hydrostatic and thermal equilibrium. In other words, the gravitational force is held up by internal radiative pressure resulting from nuclear reactions. On the other hand, the loss of heat on the surface, i.e., the luminosity, is balanced by energy originating in nuclear fusion. A pulsation is a disturbance of this fine equilibrium. Whenever a star contracts, the gravitational energy is transferred into thermal energy, thus the gas is heated up while the density increases. This leads to an increase in pressure and the star expands again. Not by the same amount, however, since a part of the energy is lost by means of radiative transfer. Accordingly, the oscillation is damped and the star reaches again a state of equilibrium after a few cycles.

In order for small perturbations to lead to macroscopic oscillations it is necessary to feed energy into the motion of the gas. One possibility is to prevent the loss of energy through radiation and to turn it into kinetic energy instead. If a large number of photons are scattered by particles like atoms, ions and electrons one speaks of a high opacity. Usually opacity decreases with an increase in temperature. However, this is not the case under special conditions. In partial ionization zones a part of the gravitational energy which is released by the contraction is fed into lifting the electrons to a higher energy level. Thus, the number of free particles is rising, resulting in an increase of opacity. The radiation is blocked and so a main part of the energy is put into the outward motion of the gas. While the star is expanding, temperature and density are falling again causing recombination and thus a decrease in opacity. Consequently, the radiation passes through more easily and the pressure will decline. The star is contracting again and the whole process is repeated. For most stars, hydrogen and helium are the main sources of opacity. In higher mass stars also the elements of the Fe group are of importance.

Since the opacity is denoted with the greek letter κ this form of driving mechanism is referred to as κ mechanism. It is important to note, that it only works in layers of partial ionization. This layer must furthermore be situated at a certain depth. If it is too close to the surface of the star, the density above the layer is too low to support the oscillations. If it is too close to the center, the gravitational force is high enough to maintain equilibrium. The most suitable conditions for the κ mechanism, working in the HeII ionization zone, occur when the star is in the area of the instability strip, i.e., when luminosity, temperature and the chemical composition of the star are in the right combination. For instance, also the pulsations of δ Scuti stars are driven by this process.

1.3 δ Scuti stars in general

The δ Scuti stars are a group of pulsators that are located in the classical instability strip on and slightly above the main sequence, as can be seen in Fig. 1.1. This means that they mostly are rather old stars, still in the phase of hydrogen core burning and evolving towards the giant branch, where they start to burn the hydrogen in their shells. However, some stars also cross the instability strip on their way to the ZAMS. Thus, there are also pre-main sequence pulsators with δ Scuti-like oscillations. The excitation mechanism responsible for pulsations in δ Scuti stars is the κ mechanism (see Section 1.2), working in the HeII ionization zone near 48,000 K (Breger, 2000a). Their masses range from $1.5 - 2.5 M_{\odot}$. From an astrophysical point of view, they are situated in a very interesting range, since a mass of $\sim 2 M_{\odot}$ is regarded as the critical mass where stars start to develop convective cores. Also, their evolutionary stage is very interesting for astrophysical research, as they move away from the main sequence. Further observing campaigns will be needed in order to test the currently inconsistent models of stellar structure.

δ Scuti stars oscillate with short periods, ranging from 18 minutes to 8 hours and rather small amplitudes from a few millimag to about 0.30 mag. However, the *high-amplitude δ Scuti stars* (HADS), which are considered a subgroup of δ Scuti stars, have amplitudes ≥ 0.30 mag (Breger, 2000a). They mainly pulsate in the fundamental radial mode and in the first and second overtone, sometimes in two of them simultaneously. However, Mathias et al. (1997) was able to detect non-radial pulsations for the HADS ρ Pup with amplitudes much smaller than that of the dominant radial mode.

Non-radial as well as radial p-modes of low order ($n \leq 7$) and a relatively high

Table 1.1: Photometrical results by Michel Breger.

	Frequency [cd^{-1}]	Amplitude [mmag]	Phase difference	ℓ
f_1	8.594	124.85	-2.67	1
f_2	5.048	115.14	-2.12	1
f_3	5.850	88.26	-6.69	2
f_4	6.976	48.55	0.38	0
f_5	5.532	68.25	-4.90	1,2
f_6	7.376	52.53	-2.69	1
f_7	7.552	43.00	-3.31	1
f_8	6.117	38.59	-5.04	1,2
f_{12}	6.680	36.68	-3.42	1

degree (up to $\ell = 20$) are generally found in δ Scuti stars. Their pulsational patterns are very complex and sometimes exhibit amplitude and phase variations. Those with shorter timescales, typically < 250 d, can be explained by simple beating of close frequency pairs (Breger, 2010). However, variations with longer timescales, which for some stars can extent to several years, are not that easy to comprehend. 4 CVn, the main object of interest for this thesis, is one example for a δ Scuti star with lengthy changes of amplitude and phase (see Section 1.4).

Breger (2000a) gives a very comprehensive review of δ Scuti pulsators. Additional information about the topic is also provided by Aerts et al. (2010).

1.4 4 CVn so far

4 CVn is an evolved δ Scuti star with a spectral type of F3 III/IV, an effective temperature of $T_{\text{eff}} = 6800 \pm 100$ K, and a surface gravity of $\log g = 3.5 \pm 0.1$ (Breger et al., 1999). Castanheira et al. (2008) found a projected rotational velocity ($v \sin i$) larger than 120 km s^{-1} , indicating that the star is a relatively fast rotator. However, during my study I was able to correct this value to be slightly lower.

Ongoing photometric observations from 1966 to 2012 made it possible to study this star in great detail and led to the publishing of various papers (Breger et al., 1999; Breger, 2000b; Breger et al., 2008; Breger, 2010). There are large gaps between the observations in the first 40 years. During the period from 2005 until 2012, 5 months per year of continuous light curves in two different wavelength ranges were

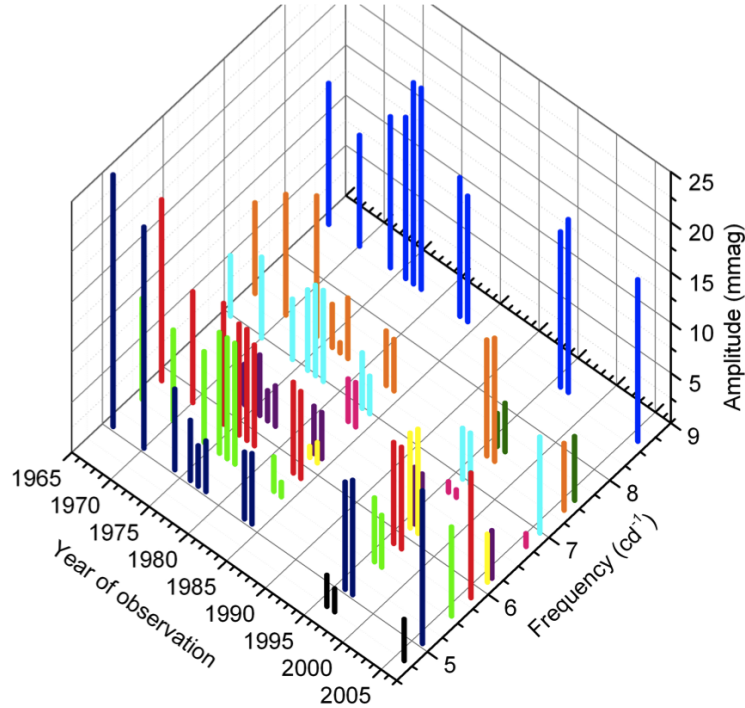


Figure 1.4: Amplitude variability for 4 CVn in the years 1966 to 2007 by Michel Breger. Each peak represents the measurement of a frequency in a year, while the respective amplitude is indicated by its height.

obtained at the Vienna Automatic Photoelectric Telescope (APT) located at Mount Washington, Arizona, USA. Their analysis revealed that the star is a very complex pulsator, exhibiting a total of 75 significant frequencies with an interesting pattern and great variability. Of 33 independent pulsation modes, 12 have amplitudes higher than 3 millimag (mmag). The temperature variations during a pulsating cycle show a strong dependence on wavelength. Therefore, multicolor photometry can help to constrain the spherical degree ℓ of the pulsations (Aerts et al., 2010). The 12 most significant modes and their ℓ value are listed in Table 1.1.

Furthermore, most of the detected modes show variations in amplitude and frequency. Figure 1.4 illustrates the variability of the amplitudes throughout the years 1966 to 2007. As already mentioned above, frequency variations of δ Scuti stars with periods smaller than 250 days can be explained by simple beating of close modes. However, there is only one close frequency pair, 6.117 and 6.1077 cycles per day (cd^{-1}) with a beat period of 107 days, which was found in the light curves of 4 CVn. All other modes have longer timescales of several years, as can be seen in Figures 1.5 to 1.9. In contrast to the amplitude variations that show no systematic behavior

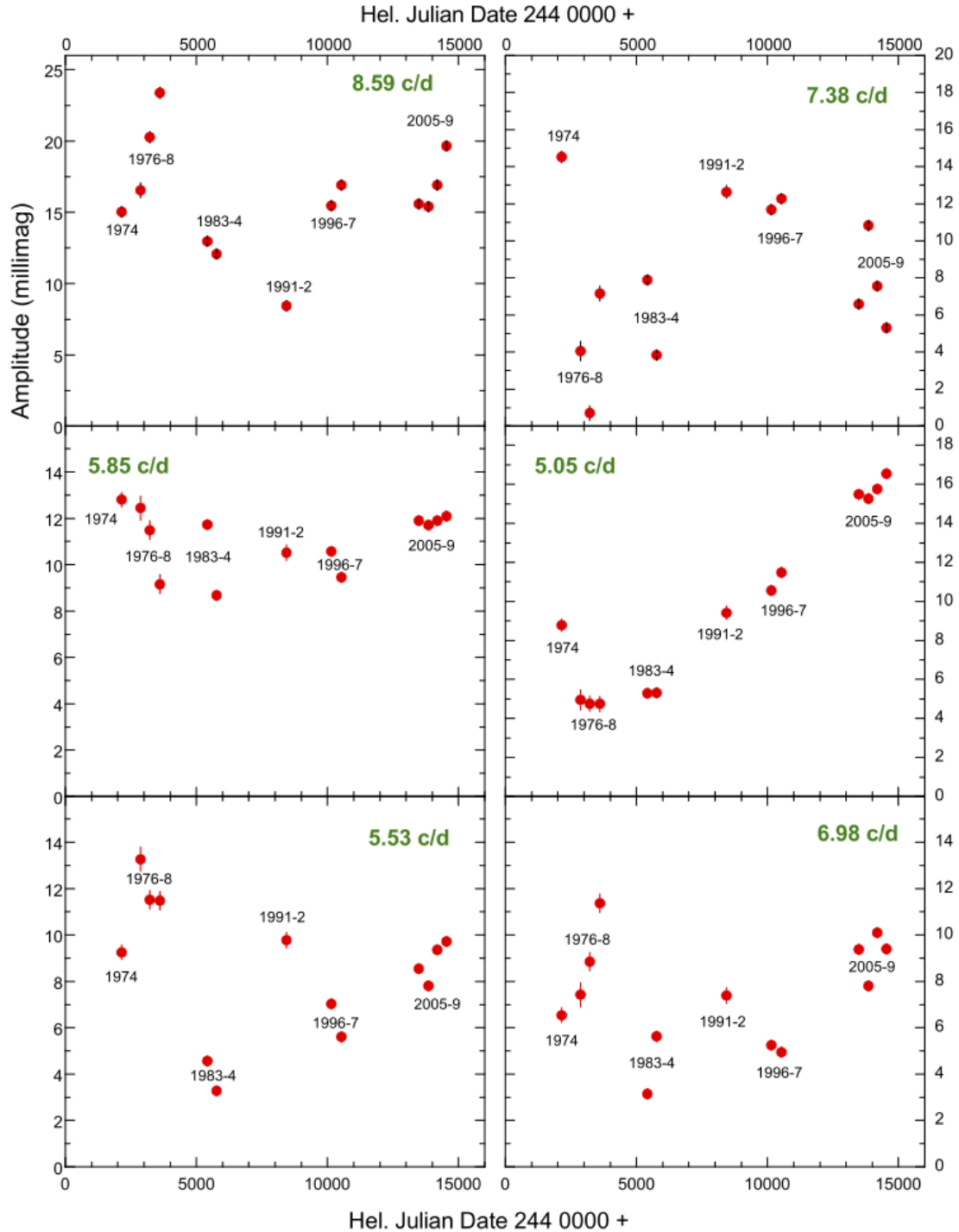


Figure 1.5: Amplitude variations of six modes of 4 CVn (Breger, 2010). No correlation between the different modes can be seen.

Table 1.2: Results of the spectroscopic mode identification by Castanheira et al. (2008).

	Frequency [cd^{-1}]	ℓ	m	χ^2
f_1	5.852	1	1	4.48
		2	1	4.65
f_2	7.374	2	-1	3.05
		1	-1	4.44
f_3	5.044	1	-1	3.32
		2	-1	3.34
f_4	8.596	2	1	1.04
		1	1	1.27
f_5	6.976	2	0	0.645
		0	0	0.697
		1	0	0.702

(see Fig. 1.5 for amplitude plots of 6 different modes), the frequency changes and phase shifts follow a clear pattern. For almost all of them, a steady rise or fall is preceded by a change in direction around the year 1990, followed by a decrease or increase in frequency thereafter.

To further investigate the properties of this pulsational pattern, an observational spectroscopic campaign was initiated in the year 2008. For more details I refer to Chapter 2. The results were published by Castanheira et al. (2008), who found 5 independent frequencies and were able to perform mode identification on each of them. They are summarized in Table 1.2. Since all of them were previously detected by means of photometry, it is possible to distinguish between retrograde and prograde modes in terms of frequency variability. For retrograde modes we can see a decrease in frequency until the sign of the slope changes around the year 1990, while prograde modes behave contrarily with a rising frequency followed by a decreasing value after 1990. Radial (or axisymmetric) modes on the other hand show very small frequency variation. Figs. 1.6, 1.7, 1.8 and 1.9 depict the frequency plots for the 5 modes which were found in both the spectroscopic and the photometric data, and which have identified degrees and orders.

Breger (2010) determines a relation between the frequency variations of the different modes. He assumes a variation in rotational splitting, since retrograde and

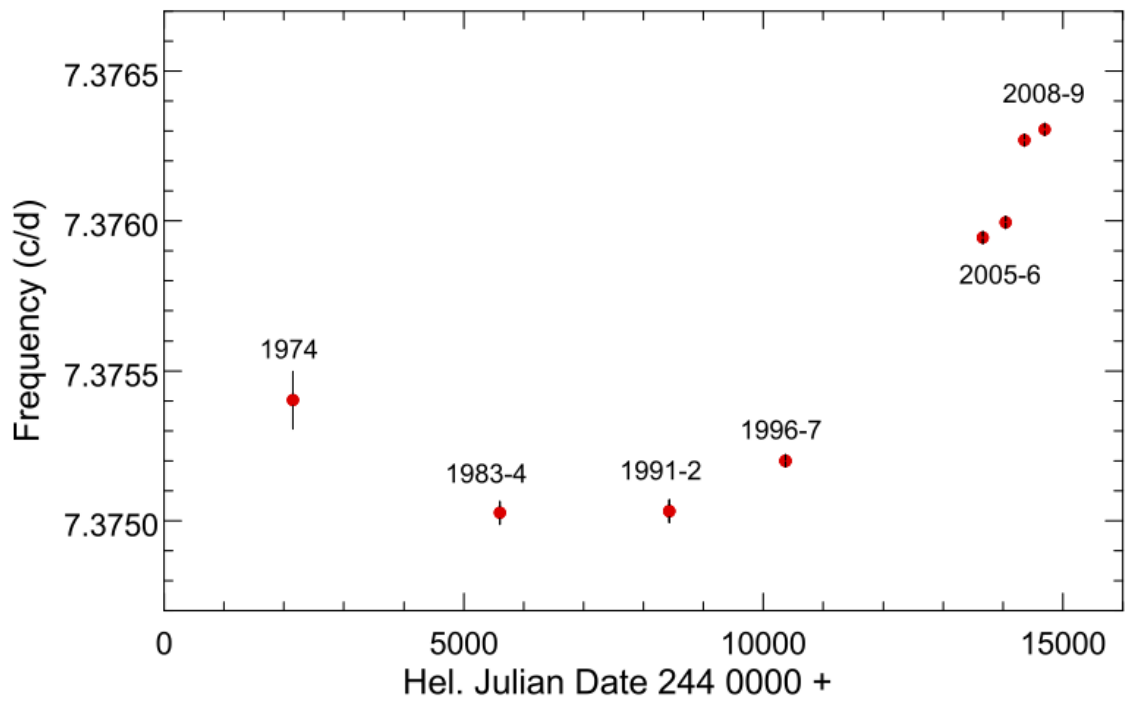


Figure 1.6: The varying frequencies of the non-radial *retrograde* mode at 7.38 cd^{-1} (Breger, 2010).

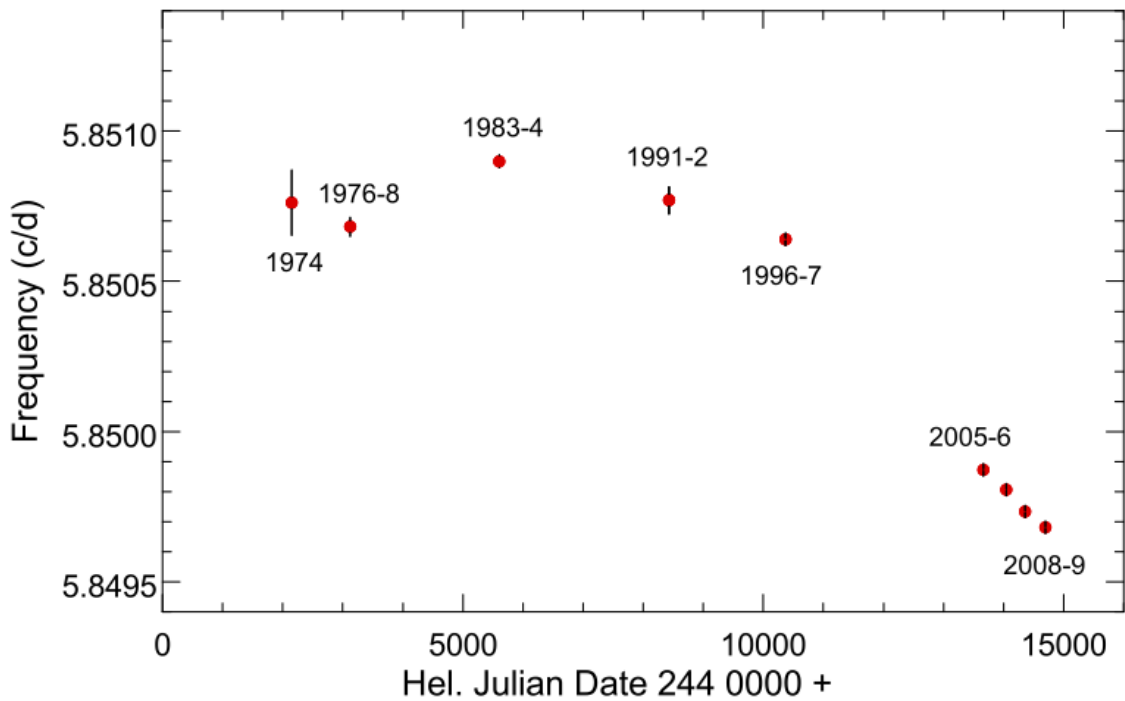


Figure 1.7: The varying frequencies of the non-radial *prograde* mode at 5.85 cd^{-1} (Breger, 2010).

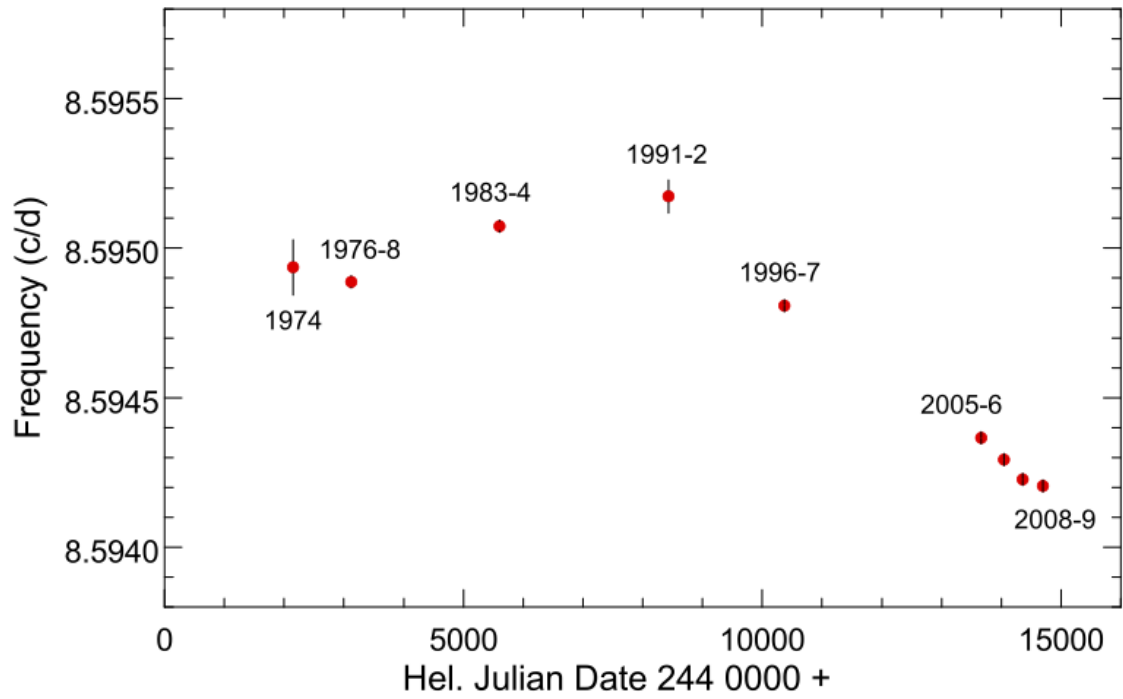


Figure 1.8: The varying frequencies of the non-radial *prograde* mode at 8.59 cd^{-1} (Breger, 2010).

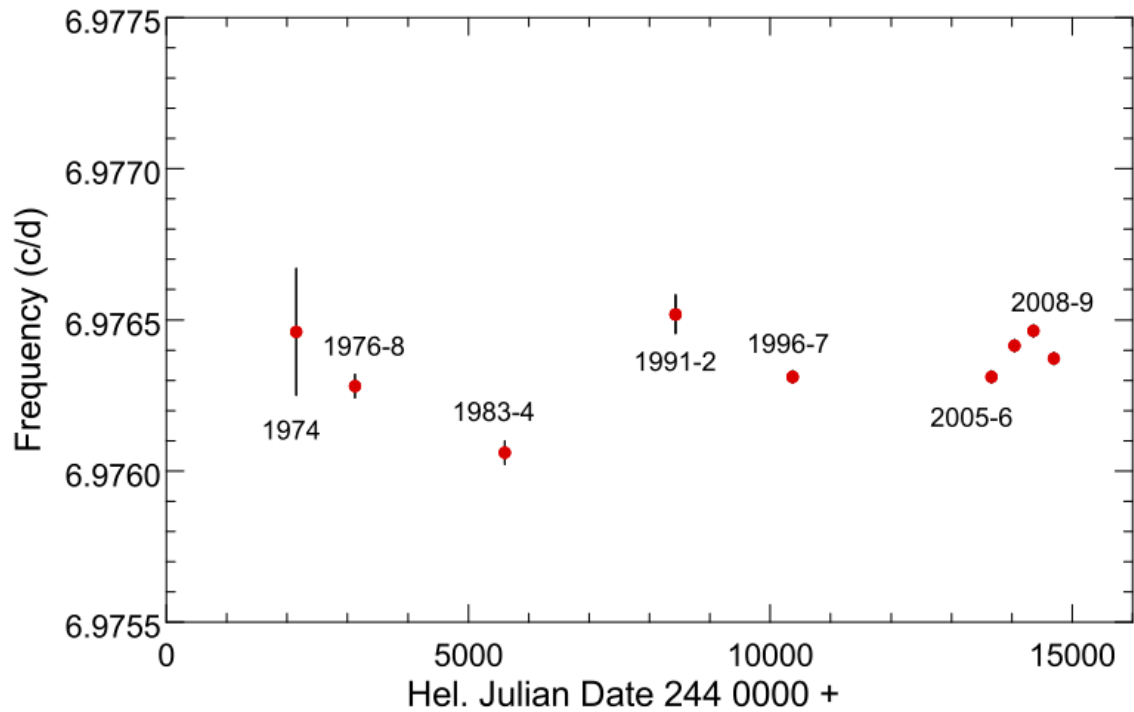


Figure 1.9: The varying frequencies of the radial mode at 6.98 cd^{-1} (Breger, 2010).

prograde modes change in exactly the opposite way while the radial mode nearly remains unchanged. This indicates that differential rotation exists and varies according to the stellar cycle. A further explanation could also be that the radius of the star is changing.

The very complex oscillations with high variability make 4 CVn a very interesting and promising target for asteroseismological studies. Due to the large amount of photometric data it is an excellent candidate for further spectroscopic research. The main goal of this thesis is to define more constraints on the parameters of the pulsation modes, which is an important requirement for prospective seismic modeling.

Chapter 2

Observations and Data Reduction

2.1 Observations

The spectroscopic observations were started in January, 2008, complementing the decades of photometric data of 4 CVn. The analysis of spectroscopic line-profile variations is a very powerful tool, which also makes it possible to detect high-degree modes ($\ell > 3$). It is very sensitive to the azimuthal order m of the pulsation modes and furthermore enables the determination of other parameters, i.e., the stellar inclination i , the projected rotational velocity $v \sin i$, the equivalent width, which is linked to the element abundance, and the intrinsic velocity amplitude of each mode (see Section 3.2.1).

Over the period of four years, data were obtained until June, 2011. To get a good picture about the amplitude and frequency variations of the spectroscopic mode, each season was analyzed separately. In this thesis I will present the analysis of the observations obtained in the season of 2010.

From February 18, 2010 to May 26, 2010 (thus, $T = 96$ d) a total of 767 stellar spectra (see, e.g., Figure 2.1) were taken over a period of 33 nights. The number of exposures per night ranges from 6 to 37 depending on atmospheric conditions and the weather. Clouds, a high wind speed, high humidity, and high particle counts for instance make it necessary to stop an observation. However, there were only seven nights during all observing runs where no spectra could be taken.

All observations were carried out at McDonald Observatory located in the Davis Mountains in West Texas, USA. We used the Sandiford Cassegrain echelle spectrograph mounted at the Cassegrain focal point of the 2.1 m Otto-Struve telescope. This instrument is a high resolution spectrograph with a resolving power



Figure 2.1: An echelle spectrum of 4 CVn taken at McDonald observatory. Every white line is one echelle order. The wavelength increases from bottom to top and from right to left, spanning a total range of 4200 Å to 4700 Å. The picket fence is the bright spot on the eighth and ninth line from the bottom. It appears twice, because the orders are overlapping. The white dots are cosmic rays.

of $R = \lambda/\Delta\lambda$ of 60,000 for a 1200×400 thinned backside-illuminated CCD chip. A continuous wavelength coverage is ensured for $\lambda < 8000$ Å (McCarthy et al., 1993). For the observation of 4 CVn for each exposure a wavelength range of 4200 Å to 4700 Å was chosen.

The Cassegrain-mounting of the instrument causes a slight shift of the echelle grating every time the telescope moves. Therefore, it is necessary to obtain calibration spectra of an integrated Thorium-Argon (Th-Ar) lamp before and after each science exposure. By identifying the Th-Ar emission lines separately for each lamp frame it is possible to subsequently track and correct the shift of wavelength in the stellar spectra (see Section 2.2). For the same reasons it is furthermore important to focus the instrument in the beginning of every night. A refocus is especially needed after every change in temperature of a few degrees and large movements of the telescope (like pointing to a new target).

Furthermore, an internal reflection of the echelle grating causes a disturbing light source in the exposures, the so-called picket fence. It is clearly visible in the spectrum shown in Fig. 2.1. This light will contaminate a small part of the CCD chip, making it impossible to recreate any information about the scientific target in this area. In order to minimize the effects of the picket fence, the grating of the spectrograph can be placed in such a way that the reflected light lies between two orders and not too close to the preferred spectral lines.

One goal of the project was to perform a mode identification, making use of the line-profile variations of absorption lines. Thus, the spectra need to meet a certain quality. First of all, it is necessary to use unblended absorption lines (see Section 3.2.1.1). Finding such lines is not a trivial task, since there are mostly blends due to the high rotational broadening at a $v \sin i > 120 \text{ km s}^{-1}$ (Castanheira et al., 2008). Castanheira et al. (2008) proposed the use of two FeII lines at 4508.288 Å and 4549.479 Å, which lie in the center of the observed spectral range and have a very high intensity. Unfortunately, the latter turned out to be highly blended by TiII at 4549.617 Å.

Furthermore, a high S/N (≥ 200), a high resolving power (above $R = 40,000$, which is provided for this instrument), and a high temporal resolution, where the ratio of exposure time to oscillation period lies below a few per cent, are required (Aerts et al., 2010). A higher S/N is ensured by higher integration times, however at the expense of temporal resolution. For 4 CVn a good balance is an exposure time between 600 s and 900 s depending on the atmospheric conditions. For the two main photometric modes ($f_1 = 8.594$ and $f_2 = 5.048$, see Table 1.1) this leads to a temporal resolution of 4% to 10% at a mean S/N of ~ 200 .

2.2 Data Reduction

The data were reduced using standard IRAF (Image Reduction and Analysis Facility) routines, following the instructions by Jeffrey and Castanheira (2010). This manual aims at the reduction of spectra taken with the Sandiford Cassegrain echelle spectrograph. However, the proposed procedure was slightly modified by adding a correction for the blaze function of the echelle grating. Also the continuum normalization was performed in a different way.

The following reduction steps were carried out:

Overscan correction The so-called overscan is a small region on the CCD which is not exposed to light. Therefore, it contains the bias level and the dark current of the instrument. By stripping and subsequent trimming of the overscan those noise levels are removed from the image. This is done using the IRAF task `ccdproc` in the package `ccdred`.

Removal of bad pixels Bad pixels are pixels that are either too bright or too dark and therefore defective. A file containing the coordinates of all bad pixels

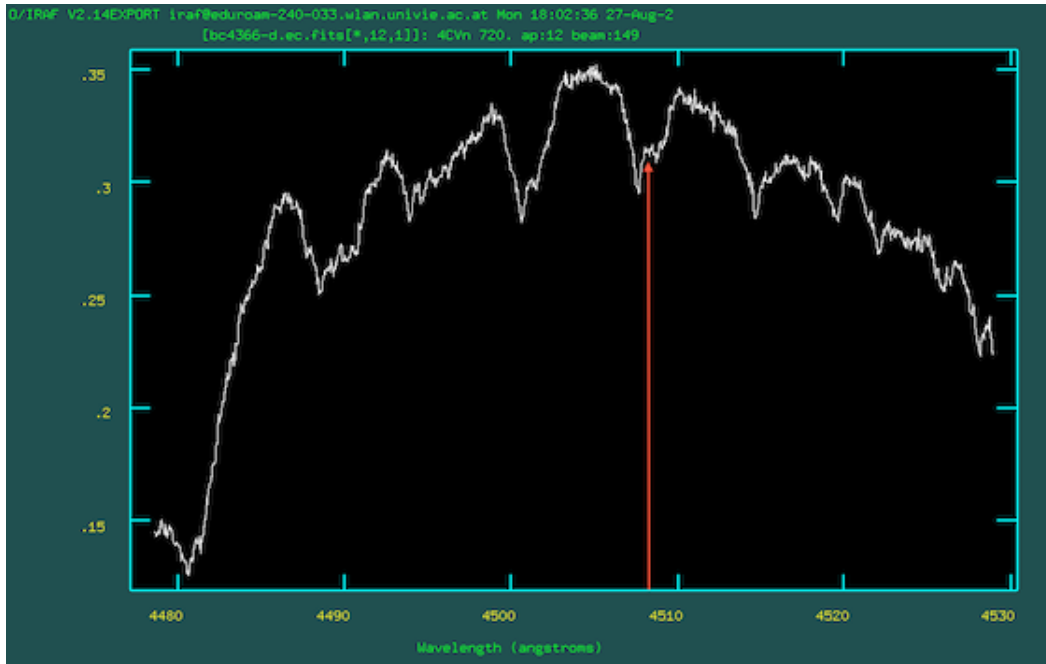


Figure 2.2: Screenshot of the twelfth order of the one-dimensional, blaze corrected stellar spectrum displayed with the IRAF task `splot` (package: `echelle`). Indicated with the red arrow is the FeII line at 4508 Å.

is provided by Jeffrey and Castanheira (2010). They are removed again using the IRAF task `ccdproc`.

Flat field correction In order to correct effects caused by the varying sensitivity of the pixels, the stellar spectra need to be divided by the masterflat file. This is a combination of all flat fields (uniformly exposed frames), created by the IRAF task `flatcombine`. For echelle data it is important to set all pixels between the orders to a unit value (task `apflatten`, package `echelle`), since they were not exposed to light and therefore have very low intensities. Firstly, the position of the orders need to be defined using the task `aptrace` in the package `echelle`. The flat field correction can then be carried out, using the normalized masterflat file and the task `ccdproc`.

Scattered light correction The residuals in between the orders are a good approximation for the scattered light. The task `apscatter` (package `echelle`) first traces the orders of the stellar spectra and secondly removes the scattered light between them.

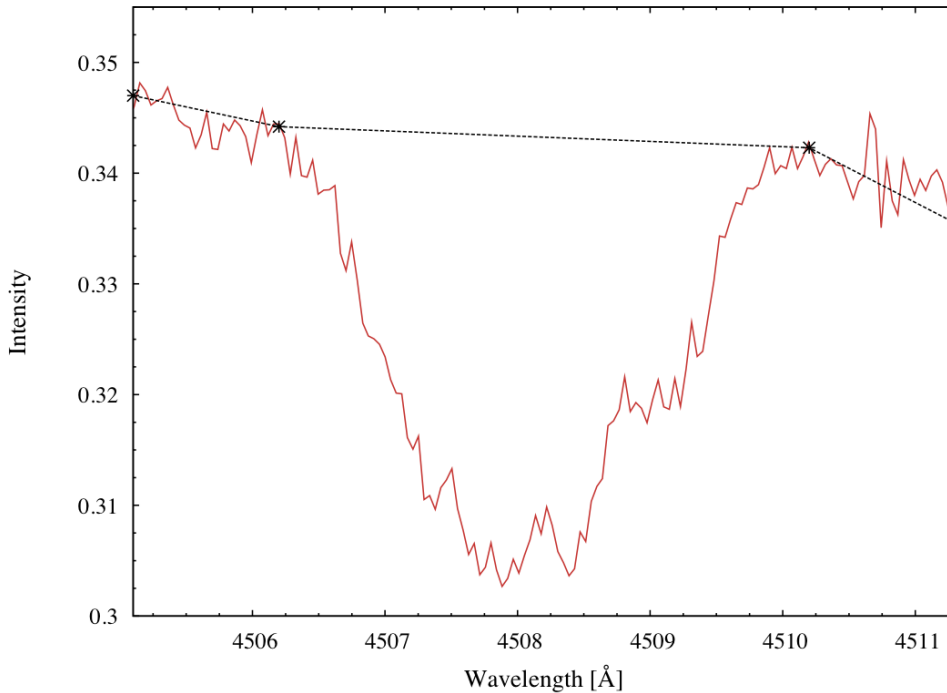


Figure 2.3: A schematic display of the normalizing points and the linear function for the FeII line at 4508 Å.

Aperture extraction All further reduction and analysis steps are performed on the one-dimensional spectra. These are created in extracting the orders with the task `apall`, also from the package `echelle`. This step needs to be carried out likewise on the science and Th-Ar frames, as well as on the masterflat.

Blaze correction This step was added to the procedure outlined by Jeffrey and Castanheira (2010). The blaze function shapes the spectrum in such a way that the maximum intensity lies at the center of the CCD chip. This is a uniform shape for the masterflat but not for the stellar spectra, since they are composed of absorption lines of different depth. For this reason, the one-dimensional science frames are divided by the one-dimensional masterflat, leading to a much smoother shape.

Wavelength calibration By comparing the one-dimensional Th-Ar spectra with an atlas of Th-Ar emission lines, a wavelength can be assigned for each line using the task `ecidentify`. It is sufficient to identify the lines in only one frame per observing run. This spectrum can then be used as a reference for all other Th-Ar frames. With the task `refspectra` each calibration frame can be assigned to one science frame, usually to the one taken right before the Th-Ar exposure. By these

means, the wavelength shift can be traced and each spectrum is calibrated correctly with the task `dispcor`.

Figure 2.2 displays the twelfth order of a fully reduced stellar spectrum. This order contains one of the absorption lines to be analyzed.

The reduced, calibrated, one-dimensional stellar spectra can now be converted into text files for further processing. Since only two FeII lines (4508 Å and 4549 Å) were used for the line-profile analysis, it was not necessary to combine the orders before converting them.

Normalization and flux calibration A special Python script was coded to perform the flux calibration on the absorption lines. Before the actual calibration process, the lines were cut from the spectra and raised to a global flux level. For the normalization, a linear function was fit through a set of points, which were predefined separately for each run. They were chosen in order to place the position of the continuum between two neighboring lines. Subsequently, the flux values of each spectrum were divided by the obtained linear function in order to shift them to a uniform level.

Heliocentric shift For the following steps it is necessary to convert the dispersion scale of the spectra from Ångström to kilometers per second. This was done using the software FAMIAS (Zima, 2008). The absorption line is now a function of radial velocity instead of wavelength.

Due to the Earth's movement around the sun, the viewing angle from the point of observation to the star is differing. Therefore, the radial velocity, i.e., the velocity of the star in the line of sight, is varying periodically. A correction value for this shift can be calculated with the IRAF task `rvcorrect` in the package `astutil`. This value was then added to the velocity scale of each line.

2.3 Binary motion

Panel a) in Figure 2.4 shows a diagram of the first line moment, which represents the radial velocity, after the heliocentric correction was applied. The strong non-sinusoidal trend still visible can be explained by a binary component. The movement of the star around the barycenter of the binary system leads to another periodic variation of the radial velocity. The second component, however, must be a very

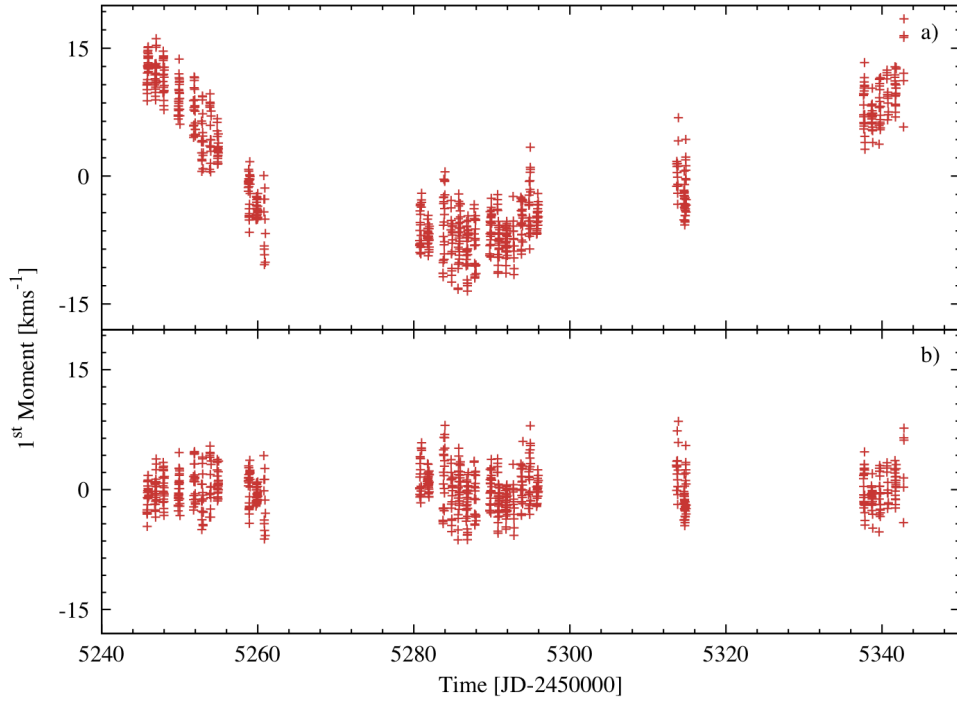


Figure 2.4: The first moment of the line 4508 Å before (panel a) and after (panel b) the correction of the binary motion.

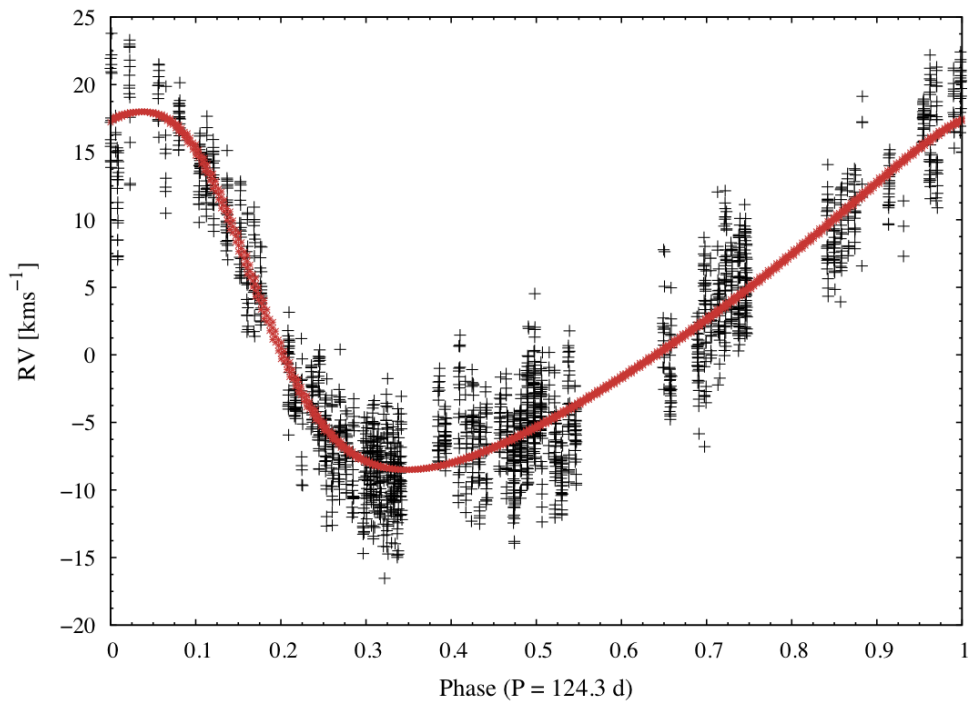


Figure 2.5: Phase diagram of the first moment of the line 4508 Å, using all spectra from 2008 to 2011. The red line represents the orbital model with a period of $P = 124.3$ days.

Table 2.1: Parameters of the orbital model.

	4508 Å	4549 Å
Orbital period [d]	124.3	125.0
Eccentricity	0.32	0.32
Systematic RV [kms ⁻¹]	3.3	2.6
Semi-amplitude [kms ⁻¹]	13.2	13.1

dim object, since the spectrum only shows absorption lines of one star.

To correct this shift, a binary model was computed by fitting a Keplerian orbit to the data (see Figure 2.5). Subsequently, the model is subtracted from the spectra. For a higher accuracy of the calculated orbit it is important to include all measurements. Therefore, also the spectra of the seasons of 2008 and 2011 were reduced according to the new procedure before the first moment was calculated for both absorption lines. The orbital parameters are listed in Table 2.1.

Since there was still a slight scatter around the zero point of the first moment, the spectra were further normalized to the average radial velocity per run. Panel b) in Fig. 2.4 depicts the first moment after all corrections were applied.

Chapter 3

Methods

Besides photometric light curves, asteroseismological analyses are also based on stellar spectra, from which stellar pulsations can be derived. In general, temporal variations, which originate from oscillations, are observed. However, it is not trivial to interpret them with respect to their nature and origin. At first it is crucial to describe the form of the oscillation, in terms of frequency, amplitude and phase, by means of a frequency analysis (explained in Section 3.1). Those characteristics can subsequently be interpreted by mode identification methods (see Section 3.2) to determine the underlying pulsation.

There exist several techniques and methods, which are not always applicable to all kinds of data and star. Thus, it is necessary to understand the mechanisms and to find the most suitable approach for the analysis of the observed data.

In this chapter I will explain the methods that were used to analyze the spectroscopic data of the δ Scuti star 4 CVn and why they seemed to be the most eligible approach. They were all implemented in a software package called FAMIAS (Frequency Analysis and Mode Identification for AsteroSeismology) by Zima (2008).

3.1 Frequency analysis

As mentioned above, it is possible to derive frequency, amplitude and phase of oscillations from time-dependent stellar properties. But which are those properties that are affected by pulsation in a periodic way?

For photometric data the situation is relatively simple. The displacement of surface elements lead to changes in temperature and radius, which in turn cause light

variations that can be observed. The resulting light curves are then studied with respect to their variations.

Stellar spectra, on the other hand, might provide much more information, but their time-dependent factors are not that easily derived. The velocity variations of the displaced elements with respect to the observer, lead to a blue or red shift in wavelengths of spectral features due to the Doppler effect. These shifts cause distorted line profiles (see Section 3.2.1), which can be studied for periodic variations. The two most common practices applied on time-series spectroscopy today are the interpretation of the variations in terms of radial velocity (see Section 3.2.2), and the separate analysis of every wavelength bin (see Section 3.2.3).

Whenever time-dependent information is extracted from the data, it can be treated just like photometric light curves. Since harmonic oscillations can be expected for δ Scuti stars such as 4 CVn, the preferred method to detect the frequencies is a Fourier transform. In order to optimize the values of amplitude and phase, a least-squares algorithm is applied. I will describe these two methods, following closely the steps outlined by Deeming (1975), who describes the Fourier analysis with unequally spaced data, and Aerts et al. (2010), who give a detailed discussion about various frequency analysis methods.

3.1.1 The Fourier transform

A good method to find the periodicity of a data set, is to approximate the temporal behavior with a series of sine functions. This can be done with the *Fourier transform* (\mathcal{FT}) which is defined for an infinite, continuous function $f(t)$ as

$$F(\nu) = \int_{-\infty}^{+\infty} f(t) \exp(2\pi i \nu t) dt, \quad (3.1)$$

This equation is transforming the function $f(t)$ from time dependence into the frequency domain, giving rise to the frequency dependent function $F(\nu)$. As $F(\nu)$ is usually complex, only its amplitude $|F(\nu)|$ is displayed and plotted against ν in a so-called *periodogram* or *frequency spectrum*. Sometimes the square of the amplitude $|F(\nu)|^2$, the *power*, is indicated in these plots instead.

In reality we are bound to deal with a series of N measurements at discrete

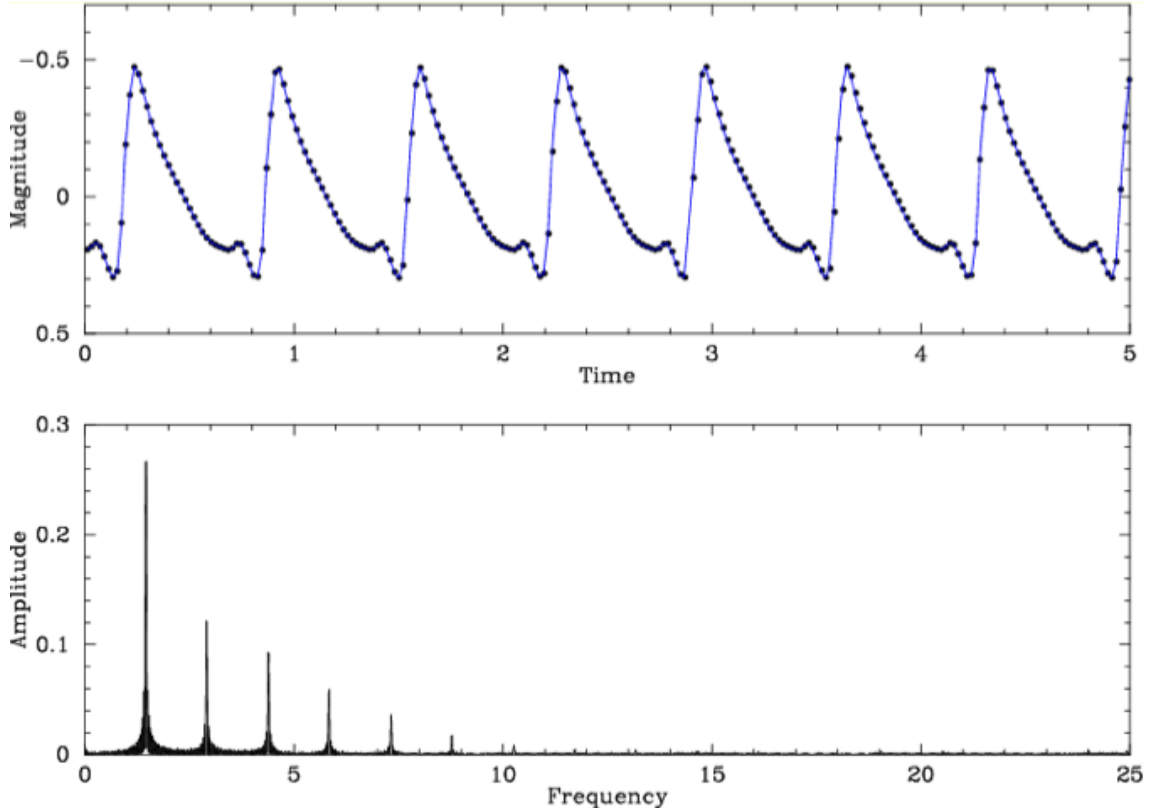


Figure 3.1: Synthetic light curve of an RR Lyrae pulsator (top panel) and its amplitude spectrum (bottom panel). The non-sinusoidal shape of the signal can only be reproduced by six sine functions with different frequencies. Taken from a lecture by Michel Breger.

points in time t_i within an interval $[0, T]$, which is far from the ideal case of infinite and continuous sine functions. Therefore, we describe the *finite* Fourier transform (\mathcal{FFT}) as an integral between the limits $t = 0$ and $t = T$:

$$F_T(\nu) = \int_0^T f(t) \exp(2\pi i \nu t) dt. \quad (3.2)$$

Taking into account a discrete distribution of points, other than the previous continuous usage, the *discrete* Fourier transform (\mathcal{DFT}), can be written by replacing the integral with a sum:

$$F_N(\nu) = \sum_{i=1}^N f(t_i) \exp(2\pi i \nu t_i). \quad (3.3)$$

Due to the definition of $F(\nu)$ according to Equation (3.1), we need to assume that the function $f(t)$ is a sum of harmonic oscillations. In other words, it is important

that the observed light curve shows a sinusoidal behavior. If the signal differs widely from this assumption, as it is the case for RR Lyrae stars, another class of pulsators, several sine functions are necessary to reproduce the shape of the light curve (see Figure 3.1), resulting in misleading incorrect frequencies visible in the periodogram. Therefore, in an ideal case, $f(t)$ can be described as a sum of M harmonic oscillations with amplitude A_k and frequency ν_k , $k = 1 \dots M$, as follows:

$$f(t) = \sum_{k=1}^M A_k \exp(2\pi i \nu_k t) \quad (3.4)$$

Subsequently the \mathcal{DFT} of this function can also be written as

$$F(\nu) = \sum_{k=1}^M A_k \delta(\nu - \nu_k) \quad (3.5)$$

where $\delta(\nu)$ is *Dirac's delta function*, which is defined as

$$\delta(\nu) = \int_{-\infty}^{+\infty} \exp(2\pi i \nu t) dt, \quad (3.6)$$

having the following properties:

$$\int_{-\infty}^{+\infty} \delta(\nu) d\nu = 1 \quad \text{and} \quad \int_{-\infty}^{+\infty} \delta(\nu - \xi) g(\nu) d\nu = g(\xi). \quad (3.7)$$

If $f(t)$ has only one frequency ν_1 (with $M = 1$), its \mathcal{FT} for a series of test frequencies will only be different from zero around the values $\nu = \pm \nu_1$. Consequently, the \mathcal{FT} of a multi-periodic function $f(t)$ will result in a series of δ -functions, i.e., that the amplitude $|F(\nu)|$ is different from zero at ν_1, \dots, ν_M .

Searching for the right frequency How can a certain periodicity of a light curve be derived using the \mathcal{FT} ? As an example we assume a signal in the form of Equation (3.4), oscillating with the frequency $\nu_1 = 3 \text{ cd}^{-1}$. For illustrative reasons we multiply the signal with the envelope function $\exp(-\pi \cdot t^2)$, which transforms the continuous sinusoid into a short impulse, as can be seen in Figure 3.2. We write $F(\nu)$ of this function with the test frequency $\nu = 3 \text{ cd}^{-1}$, following the definition in Eq. (3.1) and using the *Euler formula* $e^{ix} = \cos x + i \sin x$:

$$\begin{aligned}
F(3) &= \int_{-\infty}^{+\infty} f(t) \cdot [\cos(6\pi t) + i \sin(6\pi t)] dt \\
&= \int_{-\infty}^{+\infty} A_1 \exp(6\pi i t) \cdot [\cos(6\pi t) + i \sin(6\pi t)] dt \\
&= A_1 \cdot \int_{-\infty}^{+\infty} [\cos(6\pi t) + i \sin(6\pi t)] \cdot [\cos(6\pi t) + i \sin(6\pi t)] dt \\
&= A_1 \cdot \int_{-\infty}^{+\infty} [2 \cos^2(6\pi t) + 2i \sin(6\pi t) \cos(6\pi t) - 1] dt. \tag{3.8}
\end{aligned}$$

First we only plot the real part of the integrand, the amplitude $|F(\nu)|$ (see Figure 3.3). Whenever the real part of the signal is negative, $\Re(\exp(2\pi i \cdot 3 \cdot t))$ will be negative as well, which is why the real part of the integrand is always positive. Thus, the integral of this oscillation will produce a rather large number. On the contrary, if we try to measure a frequency that is not present in the data, the real part of the integrand will be positive and negative in almost equal parts and so integrates to a number close to zero. For example, when calculating $F(5)$ the real part of the integrand will be $2 \cos(6\pi t) \cdot \cos(10\pi t)$. Hence, the signal and $\exp(2\pi i \cdot 5 \cdot t)$ do not oscillate at the same rate anymore. The \mathcal{FT} of the “wrong” frequency is depicted in Figure 3.4.

This example illustrates that in order to find an unknown frequency in a data set, an interval of test frequencies needs to be defined to serve as an input for the \mathcal{FT} . For the lower boundary, $\nu = 0 \text{ cd}^{-1}$ is a good value, as the frequency is defined as $\nu = 1/P$ and thus an infinite period will be the limit. Moreover, the \mathcal{FT} is mirrored around zero. The upper boundary is defined by the *Nyquist frequency* ν_{Ny} .

Considering N equally spread measurements over a time span ΔT , the time separation between two data points resolves to $\Delta t = \Delta T/(N-1)$, while the sampling frequency is $1/\Delta t$. A sine curve needs to be covered by at least two points per cycle in order to resolve it from discrete measurements. Thus, half the sampling frequency is the largest frequency that can be reconstructed from the data set. This value, the so-called Nyquist frequency, is defined as follows:

$$\nu_{Ny} = \frac{1}{2\Delta t} = \frac{N-1}{2\Delta T} \tag{3.9}$$

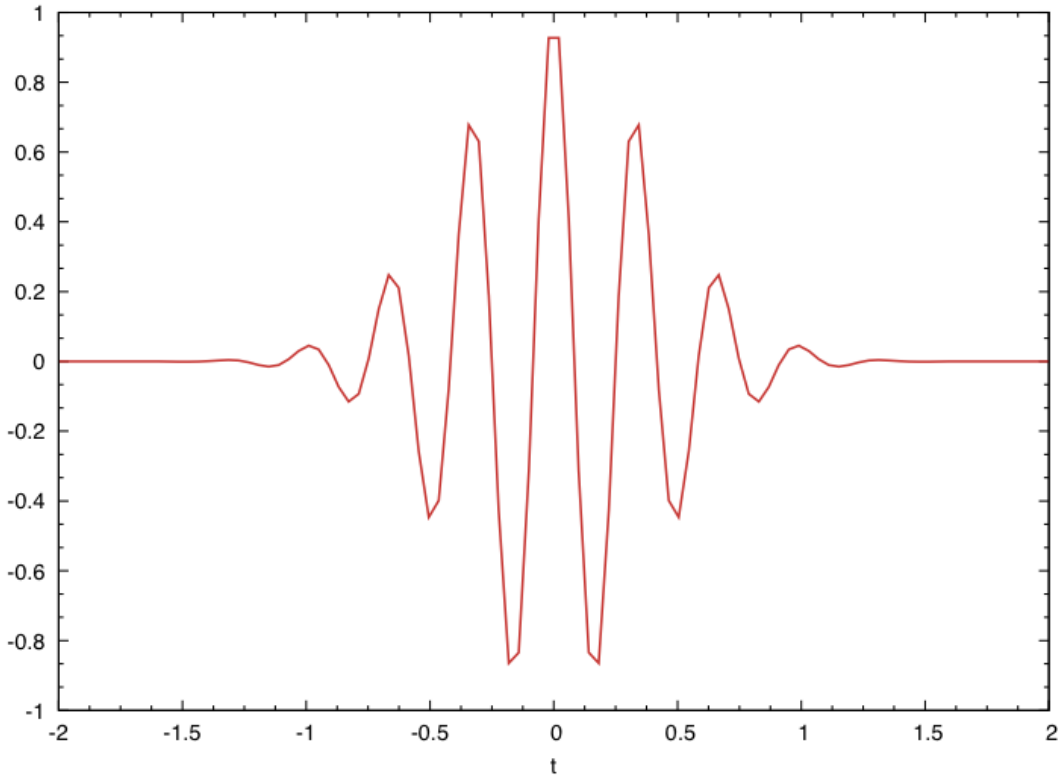


Figure 3.2: A curve according to Eq. (3.4) with a frequency $\nu_t = 3$. Its shape resembling a short pulse is produced by the envelope function $\exp(-\pi \cdot t^2)$.

3.1.1.1 The spectral window and aliasing

For $F_T(\nu)$ and $F_N(\nu)$ the periodogram does not result in a series of δ -functions, due to gaps in the observations and the limited data length. The length of the data set T results in a widening of the frequency peaks of $\simeq 1/T$. Thus, two different frequencies ν_i and ν_j will only be free of interference given that $T \gg 1/|\nu_i - \nu_j|$. A good estimate of a reliable frequency resolution is provided for $|\nu_i - \nu_j| > 2/T$. Accordingly the length of the data set plays a vital role for a good and satisfying frequency analysis.

Another strong influence on the clearness of the frequency spectrum is caused by gaps between the measurements. Naturally, astronomical observations are not equally distributed over a given time span, as the night-day rhythm, changing weather conditions, and phases of the moon regularly cause longer observing pauses. Also the Earth's orbit around the sun gives a certain limit to the continuity of the data, as most of the stars are visible during night time only for a part of the year. Collaborations between astronomers and observatories in different parts of the world,

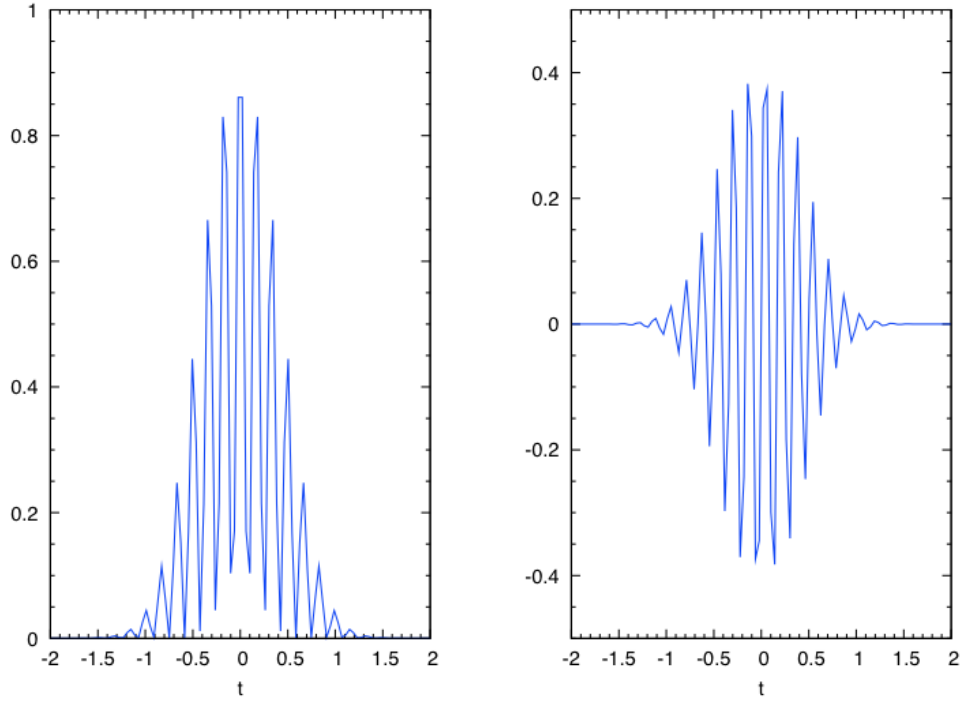


Figure 3.3: The diagram on the left-hand side shows the real part of the integrand of the \mathcal{FT} of the signal defined in Fig. 3.2 with the test frequency $\nu = 3$. The imaginary part is displayed in the right panel. Since the curve on the left side is mostly positive over t , it integrates to a relatively high value, indicating that the test frequency is the right one.

so-called multisite campaigns, are used in order to minimize the effects of the Earth's rotation. Satellite missions such as *Most*, *Corot* and *Kepler* are another effort to keep the length of the gaps to a minimum. However, this luxury of nearly continuous observations over a long period of time is still the exception rather than the rule. The data provided for this thesis are ground-based observations obtained at a single site.

Those spaces of different length allow for several oscillations of different periodicities to be fit to the data, as within them no statement can be made about the number of passed periods. Thus, they give rise to incorrect frequencies, commonly referred to as *alias frequencies*, which are visible as false maxima next to the correct frequency peak in the periodogram. Their distribution can be described by the so-called *spectral window*.

For this we first need to describe the *window function*:

$$w_N(t) = \sum_{i=1}^N \delta(t - t_i), \quad (3.10)$$

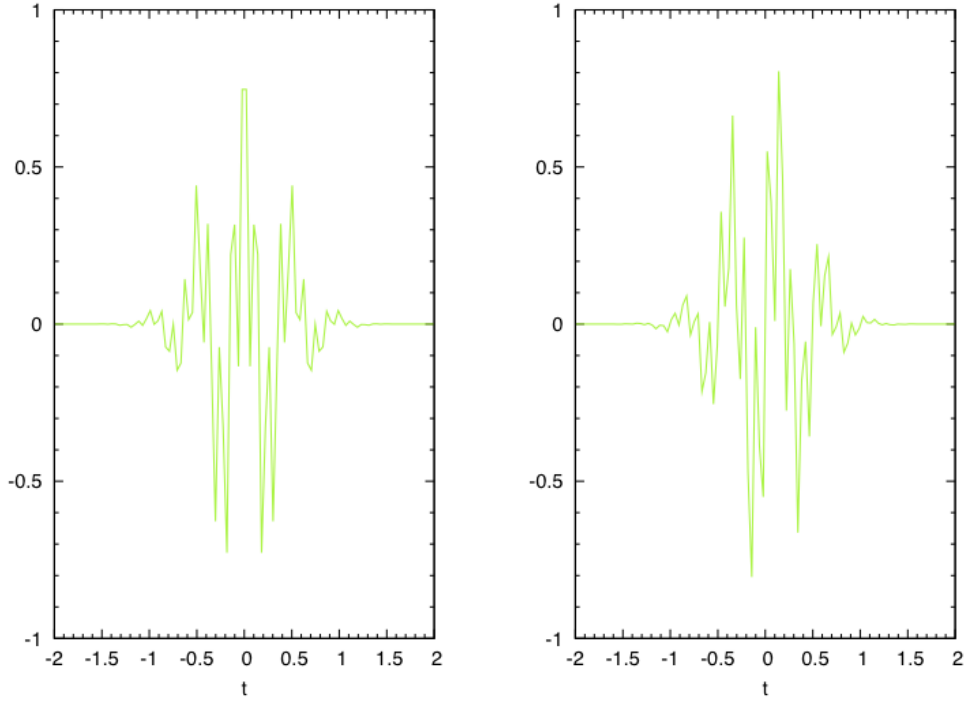


Figure 3.4: To enhance the statement made in Fig. 3.3, an \mathcal{FT} using a test frequency which is not present in the signal, in this case $\nu = 5$, was calculated. Again the real and imaginary part of the integrand are displayed in the left and right panel, respectively. This time the integral of the real part produces a much smaller value.

which is only based on the time distribution of the N data points. The spectral window then follows from the \mathcal{DFT} of the window function:

$$W_N(\nu) = 1/N \sum_{i=1}^N \exp(2\pi i \nu t_i). \quad (3.11)$$

$F_N(\nu)$ is a convolution of $F(\nu)$ and $W_N(\nu)$:

$$\frac{F_N(\nu)}{N} = (F * W_N)(\nu) = \int_{-\infty}^{+\infty} F(\nu - \nu') \cdot W_N(\nu') d\nu'. \quad (3.12)$$

As stated above, $F(\nu)$ is a δ -function at frequency ν_1 for a mono-periodic oscillator. Hence, taking into account the properties of the δ -function described in Equation (3.7), we can write $F_N(\nu)/N = W_N(\nu) * \delta(\nu - \nu_1) = W_N(\nu_1)$, corresponding to the same shape of the \mathcal{DFT} as the spectral window centered around ν_1 . If $F(\nu)$ is a sum of M δ -functions, $F_N(\nu)$ will be the sum of M spectral windows centered around the different frequencies ν_1, \dots, ν_M .

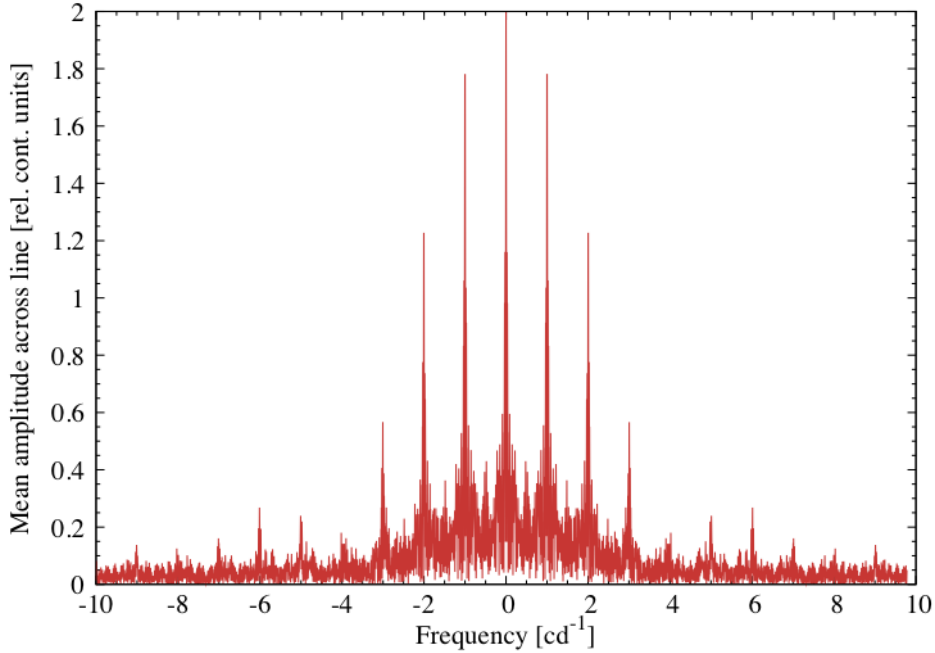


Figure 3.5: The spectral window for the data set of the year 2010, which was analyzed for this thesis. The side lobes at $\pm 1, 2, \dots$ days are due to one-day aliasing.

Let us now examine the spectral window more closely. As alias peaks are caused by the uncertainty of periods occurring within or between the gaps, it is obvious that gaps appearing with a certain periodicity will allow for strong aliasing. Observational breaks occurring clearly periodically are of course the above mentioned daily breaks and seasonal visibility of the star in the night sky, giving rise to the most common alias frequencies, the so-called *one-day aliasing* and *one-year aliasing*. The daily side peaks occur with a period of multiples of 1 d at frequencies $\pm 1, \pm 2, \dots \text{cd}^{-1}$, while the annual aliasing will have a periodicity of multiples of ~ 365 d and thus appear at a step rate of $\pm 0.00274 \text{cd}^{-1}$. Figure 3.5 shows a plot as defined in Equation (3.11) for the data set used for this thesis. Both the one-day and the one-year aliases are clearly visible.

The diagram is centered around zero, within a range $\pm \nu_i$, because the resulting frequency spectrum is comparable to the spectral window centered around the value ν_1 . Obviously, the aliasing has a large effect on the surroundings of the correct frequency peaks, as they not only spread in positive but also in negative direction. Hence, as each frequency is convolved with the spectral window, the periodogram of a multi-periodic pulsator will be subject to interference. The spectral window should therefore always be studied thoroughly before any statements can be made

about the periodicity of the data.

3.1.2 Least-squares fit

As a next step, the frequency found by the means of a Fourier transform is improved by applying a least-squares algorithm. Also, amplitude and phase can be determined within an error range.

Similar to the idea of the Fourier analysis described in the previous section, this method is used to find harmonic oscillations in a signal. This is achieved in minimizing the squared errors between the model and the data. Thus, we describe an ideal case of N measurements $x(t_i) \equiv x_i$ at time points t_i , $i = 1, \dots, N$ of a signal consisting of M sinusoidal oscillations with frequency ν_k , $k = 1, \dots, M$:

$$x(t_i) = \sum_{k=1}^M a_k \cos[2\pi\nu_k(t_i - \tau)] + b_k \sin[2\pi\nu_k(t_i - \tau)] + c + \varepsilon_i. \quad (3.13)$$

Here τ describes the epoch of the observations, ε_i the measurement errors, and a_k, b_k and c are free parameters defining the curve.

The unknowns that we want to determine in the best manner are ν_k, a_k, b_k and c .

3.1.2.1 Mono-periodic signals

The simplest case is a light curve with only one oscillation mode at a frequency ν_1 , with $M = 1$, $a_1 = a$, and $b_1 = b$. In order to determine this frequency, we define a model oscillation with the test frequency ν and express the squared deviations to the signal as follows:

$$L = \sum_{i=1}^N \{x_i - a \cos[2\pi\nu(t_i - \tau)] - b \sin[2\pi\nu(t_i - \tau)] - c\}^2. \quad (3.14)$$

First we need to form and solve the derivations $\partial L/\partial a = 0$, $\partial L/\partial b = 0$ and $\partial L/\partial c = 0$ to find the unknown variables a, b, c . This allows us to calculate the value $x_i^c(\nu)$ for the point t_i , an epoch τ and the test frequency ν in the way:

$$x_i^c = a \cos[2\pi\nu(t_i - \tau)] + b \sin[2\pi\nu(t_i - \tau)] + c. \quad (3.15)$$

The best frequency ν is determined by comparing the observations and the predictions and minimizing the sum of their squared deviations or *residuals* $R_i(\nu)$.

Thus, for a time t_i we write the difference between the measured and the calculated value as

$$R_i(\nu) = x_i - x_i^c(\nu). \quad (3.16)$$

And subsequently for the sum of their squares

$$R^2(\nu) = \sum_{i=1}^N R_i^2(\nu) = \sum_{i=1}^N [x_i - x_i^c(\nu)]^2. \quad (3.17)$$

Since a, b, c are complex variables difficult to describe, we choose another form for $x_i^c(\nu)$, namely:

$$x_i^c = A \cos\{2\pi[\nu(t_i - \tau) + \delta]\} + c \quad (3.18)$$

where A is the amplitude, δ is the phase and ν is the frequency. These are quantities that can be observed and are thus more intuitive than the arbitrary a, b and c . Using Equation (3.18) a least-squares approach is carried out once more to receive a model with test values for amplitude, frequency, and phase that describe the signal best.

According to Equation (3.16), the residuals $R_i(\nu)$ are the differences between observation and the predicted value. Furthermore, we describe the variance σ_i^2 as the square of the standard deviation scaled with N or $\sigma_i^2 = (x_i - \bar{x})^2/N$. Hence, a comparison between those two quantities can also be understood as a comparison between the best and the worst model. This allows a measurement of the accuracy of the predictions, also called *variance reduction* or *fraction of the variance* (f_ν), i.e., the fraction of the variability that can be explained by a model. We write f_ν as:

$$f_\nu = 1 - \frac{\sum_{i=1}^N (x_i - \{A \cos(2\pi[\nu(t_i - \tau) - \delta]) + c\})^2}{\sum_{i=1}^N (x_i - \bar{x})^2} = 1 - \frac{L}{\sum_{i=1}^N (x_i - \bar{x})^2}, \quad (3.19)$$

where $\bar{x} = \sum_{i=1}^N x_i/N$ is the average of x_i . Obviously, for minimized residuals, L is close to zero and therefore much smaller than the variance σ_i^2 , which results in f_ν being close to one. Thus, the calculated value x_i^c with the amplitude A , frequency ν and phase δ describes the variability of the signal very well.

3.1.2.2 Multi-periodic pulsations

In the case of a multi-periodic pulsator, we assume a signal of harmonic oscillations of M different frequencies ν_k , $k = 1, \dots, M$ (see Equation 3.13). Naturally, we want to apply the same procedure as in the example of a light curve with one periodicity explained above. Since we cannot predict how many modes have an amplitude above the detection limit, we also do not know M and we therefore have to determine it along with the different frequencies. However, the estimation of discrete parameters is still very difficult and it represents until now a not well developed field in statistics.

An attempt to avoid this problem is to perform a *prewhitening* after each search for a frequency. Therefore, a fit for the best frequency is calculated and subsequently subtracted from the data, before another search is started. The best value is selected in adopting a minimal value of the residuals by means of Eq. (3.16). However, to obtain the best possible fit, it is necessary to include each so far determined frequency in the calculations. While the frequency can be set as a fixed value, amplitude and phase are used as free parameters to avoid systematic errors. After each prewhitening-step another frequency search is performed. The least-squares calculation is used with frequency, amplitude and phase as free parameters this time. Usually a good starting value for ν_k is determined by means of another method, such as the Fourier transform, described above.

3.1.3 The significance of the frequencies

As the search for the oscillation frequencies is performed in an iterative way, and the number of excited modes M is unknown, a reliable stop criterion needs to be defined. An obvious assumption would be to stop as soon as all intrinsic frequencies have been extracted from the data. The difficulty lies in distinguishing between the peaks caused by stellar pulsation and mere noise. If the amplitude of the candidate frequency is significantly higher than the mean amplitude of the surrounding noise, it is more likely to originate from oscillations of the star.

Breger et al. (1993) argue that a critical value for the signal-to-noise amplitude ratio (S/N) is ~ 4.0 . Later, Kuschnig et al. (1997) have confirmed this significance level and stated for data obtained with the Hubble Space Telescope Fine Guidance Sensors, which are mostly limited by photon noise, peaks above the critical value of 4.0 times the mean noise amplitude are intrinsic to the star with a probability of 99.9%. In order to avoid distorting the noise level by alias peaks accompanying the candidate frequency, it is necessary to calculate the noise amplitude only after

the removal of every previously detected frequency and within a reasonable region around the peak in question. Once the amplitudes of the highest frequency peaks lie below the critical S/N level, it can be assumed that all detectable oscillation frequencies M have been extracted from the data.

If the amplitude of the frequency and the one of its aliases are very similar, it can no longer be distinguished between the two. The ratio of these amplitudes largely depend on the duty cycle in such a way that it is much smaller for a smaller data coverage over time.

3.2 Mode identification

With the analysis of the periodic variations of observables, one is able to describe the oscillations of a star. However, the nature of the pulsations and their origin cannot be explained by frequency, amplitude, and phase alone. The geometry of a mode, which is represented by the quantum numbers ℓ and m , allows to trace the ray path, which in turn largely depends on the internal density profile and the chemical composition of the star.

Mode identification is a method to derive values for (ℓ, m) for each individual mode. Several techniques were developed in the course of the history of asteroseismology, each specified for the type of the derived data and the different properties of pulsating stars, like the rotational velocity. Here I will present two techniques commonly applied to spectroscopic data, focussing on the Fourier parameter fit method, which is especially suitable for fast rotating stars. It is an enhancement to the pixel-by-pixel method and was developed by Zima (2005) for his PhD thesis.

Stellar spectra provide a large amount of specific information about the observed star, especially in the profiles of absorption lines. Thus, the fitting of these profiles with theoretical values, allows the determination of not only (ℓ, m) , but also of certain stellar parameters and line attributes. Among them are the projected rotational velocity $v \sin i$, the inclination i , i.e., the angle between the rotational axis and the line-of-sight, the equivalent width EW , the intrinsic width σ , and the intrinsic pulsational amplitude v_p of each mode.

However, to use the full capacity of modern mode identification techniques, it is crucial to obtain highly resolved ($R > 40,000$) spectra with a high signal-to-noise ratio ($S/N > 200$). In order to fully resolve the oscillations over one period, it

is furthermore necessary to keep the ratio of the exposure time to the pulsation cycle to a minimum (Aerts et al., 2010). Hence, larger telescopes with sensitive instrumentation are needed for a longer period of time to achieve the desired quality for the data. As this is still a hard task, it is recommended to combine the advantages of different techniques. For example, multicolor photometry is able to give a good constraint on the harmonic degree ℓ , and the analysis of line profile variations is more sensitive to the azimuthal order m . There already exist large amounts of photometrical studies for the δ Scuti star 4 CVn, as mentioned in Section 1.4. We are now able to find a detailed description for its pulsation modes, by combining the information of previous studies with spectroscopic results.

3.2.1 Line-profile variations

This section summarizes the origins of line-profile variations. For a detailed discussion on this topic and line-profile fitting I refer to Aerts et al. (2010) and Zima (2005).

The variation of the profile of absorption lines originates from the perturbed surface of a pulsating star. With these spectroscopic data it is possible to identify the quantum numbers (ℓ, m) of pulsation modes. Absorption lines are a characteristic signature of the transitions of electrons between the different energy levels of atoms. Usually, these transitions are caused by the absorption of stellar photons in the atoms or ions. The lines occur at certain ranges of wavelengths of stellar spectra, depending on the energy of the absorbed photon. The shape, however, is subject to the physical conditions of the region where the line is formed, i.e., temperature, pressure, gravity, and element abundance.

An important characteristic is the *equivalent width* (EW) of a line: it is defined as the width of a rectangle with unit height and the same area as the line. It is sensitive to the totally absorbed energy and thus, a measure for the element abundance in the region.

Several conditions cause a broadening of the line, their combined effect is called *intrinsic width*. One of its components is the *natural* or *atomic broadening*. It is due to the finite lifetimes of the excited states of the electrons and the significant uncertainty of the measurement of energies necessary for the extremely short lived transitions that can be described with the uncertainty principle. This effect results in a Lorentz profile.

The line shape is furthermore altered by the presence of nearby particles. As the density of the particles and hence the frequency of such encounters strongly

depends on the pressure, this effect is called *pressure broadening*. On the one hand, the collisions of particles shortens the lifetimes of energy levels and thus enhances the uncertainty of the involved energies. On the other hand, the mere presence of neighboring particles alter the energy levels and thus shift the frequency of the line. The pressure broadening can also be represented by a Lorentz profile.

The last considered effect contributing to the intrinsic width is the so-called *thermal broadening*, which can be approximated by a Gaussian profile. The thermal energy of the gas results in microscopic movements of the particles, whose emitted frequencies are subsequently Doppler shifted by the value $\Delta\lambda$, defined as

$$\frac{\Delta\lambda}{\lambda} = \frac{v}{c}, \quad (3.20)$$

where λ is the laboratory wavelength, v is the velocity and c is the speed of light. Because of the statistical distribution of the thermal motion of particles the Doppler effect results in a broadening of the line. Moreover, this effect is strongly dependent on temperature, because with increasing temperature the agitation of the particles increases, too. On a macroscopic scale, turbulent motions like convection have to be taken into account and result in a further broadening, represented again by a Gaussian profile.

Thus, the intrinsic width is the convolution of a Lorentz and a Gaussian profile, which results in a Voigt profile. For mode identification, however, the approximation of the intrinsic line shape with a Gaussian is sufficient with benefit for the computational time.

In addition to these local effects originating from the conditions in a small region around the absorbing element, the line shape is altered by more global effects. These are *rotational broadening* and stellar oscillation, which both are a result of the Doppler effect similar to thermal broadening.

The rotational broadening is caused by the rotation of the star. For a uniform, time-independent rotation, the velocity fields on the opposite sides of the stellar disc have a different direction. Therefore, the line is symmetrically broadened depending on the rate of rotation. A high rotation rate leads to broader lines.

Furthermore, the line varies periodically with non-radial oscillations of the stellar sphere. Depending on the pulsation mode, the quantum numbers (ℓ, m) , the amplitude of the oscillation, the ratio between horizontal and vertical components of the pulsational amplitude k , and the stellar inclination i , the shape of the line is altered in a way that the center shifts from one side to the other and bumps move

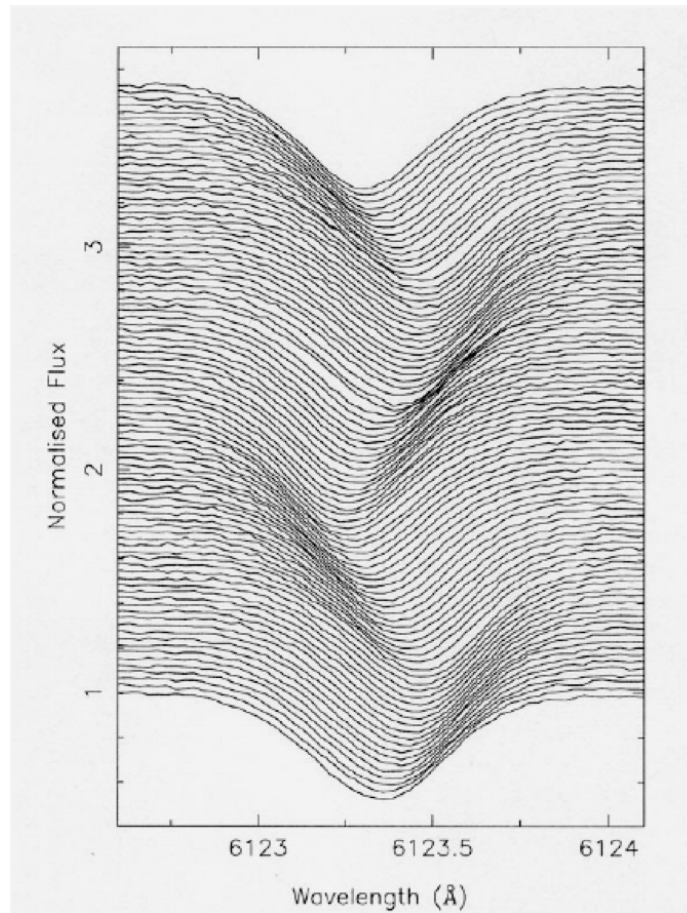


Figure 3.6: Line-profile variations of the δ Scuti star ρ Puppis. The star was observed with the Coudé Echelle Spectrograph at the 1.4 m CAT Telescope at ESO (La Silla, Chile) in 1995 and published by Mathias et al. (1997).

periodically across the line. The displacement of the line forming region due to the pulsation, moreover, causes a change in effective temperature, pressure and density, which is higher for more rapidly rotating stars. Since most of the discussed broadening effects are sensitive to temperature, this change will result in a variation of the line's equivalent width. All these factors will lead to the so called *line-profile variations* (LPV). Figure 3.6 displays the temporal variations of the CaI line at 6122.21 Å for the δ Scuti star ρ Puppis (Mathias et al., 1997).

3.2.1.1 Selection of lines

Not every line is eligible for frequency analysis and mode identification, because certain criteria have to be fulfilled. Here I am following the selection process by

Zima et al. (2006).

Most importantly, the absorption line has to be unblended, i.e., it must not overlap with any other atomic or molecular line. In other words, the signature of the pulsation across the line profile has to originate from one element only, without being contaminated by any other features.

Another important property of the line is a great depth and sharpness, as in this case the LPVs are more pronounced (Aerts et al., 2010). Metal lines are therefore to be favored over hydrogen or helium lines. However, metal absorbers may be sensitive to small local temperature changes, which, as explained above, can result in EW variations. Since these variations have to be taken into account for mode identification, it is advisable to choose lines which show no time dependence in EW .

De Ridder et al. (2002) studied the temperature and EW variations of slowly pulsating B stars and slowly rotating β Cephei stars using the SiIII doublet and the SiIII triplet around 4130 Å and 4560 Å, respectively. Only for a few targets they found a clear harmonic signal in EW . For the other objects the EW phase diagrams had a strong scatter due to multi-periodicity. Hence, the used silicon lines are mostly insensitive to temperature variations and thus very suitable for mode identification in B stars. They further argue that the EW variations are therefore not adequate enough to study the pulsation modes of B stars. Unfortunately, for δ Scuti stars no investigations of similar accuracy concerning the temperature dependence of absorption lines have been conducted so far (Aerts et al., 2010).

If more than one line should be used for the analysis, it is important to choose absorbers which have a similar behavior over time. Thus, it is best to use lines originating from the same element in preferably the same ionization state. This is of especial importance when the lines are to be combined in order to achieve a higher S/N (Zima et al., 2006).

3.2.2 The moments of the line

The n -th moment in integration is defined as the integral over the product of a variable to the power n and a function of this variable. The moments of the line profile $I(v, t)$ at a time t , as a function of the velocity v can therefore be written as follows:

$$\langle v^n \rangle_I(t) = \frac{\int_{-\infty}^{+\infty} v^n I(v, t) dv}{\int_{-\infty}^{+\infty} I(v, t) dv} \quad (3.21)$$

(Zima, 2005). Here, v represents the Doppler velocity, a combination of pulsational and rotational velocity in a certain region on the stellar surface.

In theory all moments are necessary in order to reproduce the whole information that can be extracted from the line profile. In practice, however, the first three moments contain the most important information and are usually sufficient for the purpose of mode identification. Also, the noise increases with increasing order of the moments and is higher for even moments, compared to odd moments. Moreover, they can be explained with the following physical properties:

- The first moment can be explained as the centroid of the line and the average velocity in the line-of-sight, i.e., the radial velocity.
- The second moment measures the variance across the line.
- The third moment represents the line's skewness.

The *moment of order 0* is a measure for the equivalent width and, moreover, is the denominator in Equation (3.21). Hence, all moments are normalized to EW and therefore corrected for small changes in temperature and flux (Aerts et al., 2010; Zima, 2005).

3.2.2.1 Frequency analysis and mode identification with the moments

All further temporal variations of the moments can now be interpreted as signatures of the stellar pulsation. The frequency analysis methods explained above are applicable and by these means, the oscillation frequencies can be detected.

The theoretical expression for the line-profile variations $I(v, t)$ in Eq. (3.21) can be calculated from a set of equations. Thus, the pulsational quantum numbers (ℓ, m) can be identified. These calculations are explained completely by Aerts et al. (1992). The moments computed from an observed series of spectra can then be compared to the theoretical moments. By minimizing a discriminant, a good estimation of certain parameters ($\ell, m, v_p, i, v \sin i$ and σ) can be made.

The moment method is more sensitive to low-degree modes ($\ell \leq 4$), as was determined by de Pauw et al. (1993) in an accuracy test. Especially the first moment is subject to partial cancellation effects, which lead to smaller amplitudes for modes with $\ell > 4$. Furthermore, Aerts et al. (1992) state that this method only works for slowly rotating stars ($v \sin i \leq 50 \text{ kms}^{-1}$).

3.2.3 The Fourier parameter fit method

The main idea of the Fourier parameter fit method (FPF), developed by Zima (2005) as an enhancement to the pixel-by-pixel method, is to analyze the variation of the line profile for each wavelength bin separately. Thereby, the temporal variation of each bin is transformed into the frequency domain by means of a Fourier analysis (see Section 3.1.1). In this process a two-dimensional amplitude spectrum is produced, showing not only the variation of amplitude as a function of frequency, but also across the entire line profile. Figure 3.7 shows such an amplitude spectrum. A more practical approach, however, is the analysis of a one-dimensional amplitude spectrum (see right-side plot of Fig. 3.7). This can be obtained by calculating the mean amplitude for each frequency across the line. Since all variations are integrated over the entire profile, this method is very sensitive to high-degree modes ($\ell > 4$). This is a main advantage compared to the moment method (see Section 3.2.2), which is much more prone to partial cancellation effects.

After all significant oscillation frequencies have been detected, the Fourier parameters can be determined by means of a least-squares fit. These are the zero point Z_λ as well as the amplitude A_λ and the phase ϕ_λ across the line. By keeping the frequency constant, it is possible to calculate the deviations from wavelength bin to wavelength bin of A_λ and ϕ_λ . These results will later be used for mode identification.

The parameters of the pulsation modes can be determined by comparing the observed values to theoretical expectations of A_λ and ϕ_λ , as shown in Figure 3.8. Therefore, a theoretical line profile needs to be calculated and a model fitting for amplitude and phase are derived. A goodness-of-fit parameter then determines the model that provides the best approximation of the variation of A_λ and ϕ_λ . However, it is not possible to pinpoint the correct solution among several models that all fulfill a certain goodness of their fit. To remedy this handicap, Zima (2006) introduced a χ^2 -test (explained below in more detail) to the method in order to distinguish between the best fitting models. A genetic optimization algorithm is applied to ensure a precise and reliable selection process. This makes the FPF method a very

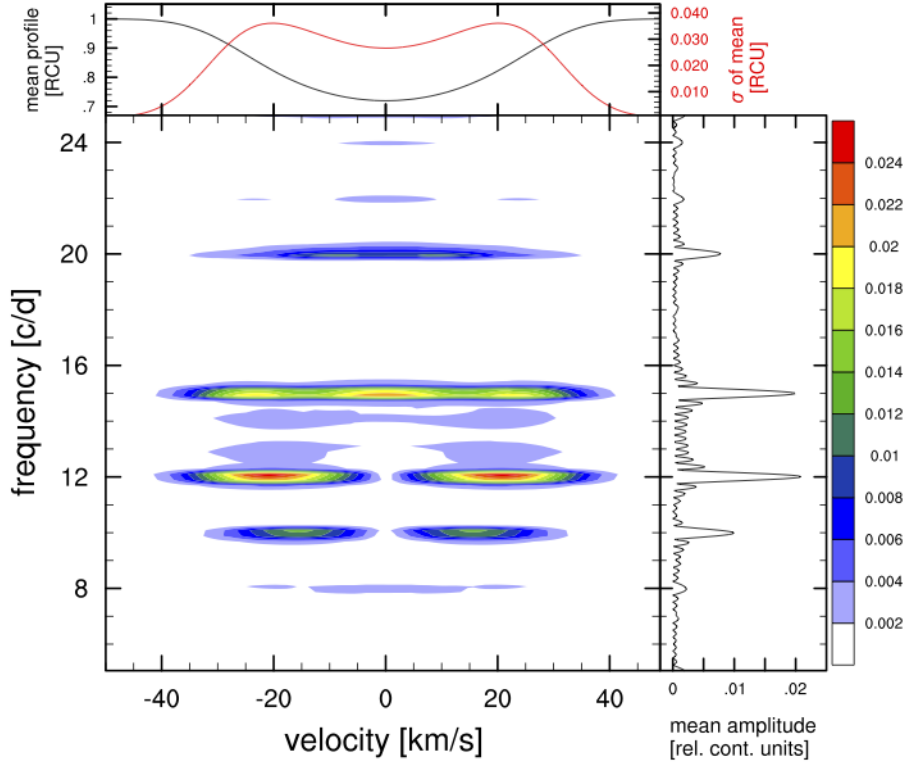


Figure 3.7: A two-dimensional Fourier transform of the pixel-by-pixel variations of a spectral line. The amplitude is coded with the color scheme shown on the right-hand side of the diagram. The top panel displays the mean line profile in black and the standard deviation of the mean in red. The diagram on the right displays the one-dimensional frequency spectrum, i.e., the average amplitude across the pixels for each frequency. Diagram taken from Zima (2005).

robust technique for mode identification, furthermore allowing the calculation of the parameters ℓ , m , v_p , i , $v \sin i$ and σ .

As the variations in the line profile are studied in great detail, it is crucial to obtain spectra of high resolving power and a good S/N. A high stellar rotation ($v \sin i > 50 \text{ km s}^{-1}$) is of further importance, since the rotational velocity leads to an additional broadening and therefore better resolved features within the line.

3.2.3.1 Chi-square test

A χ^2 -test tries to find the goodness of the fit of a theoretical model to an observed sample, assuming the validity of the null hypothesis. This hypothesis says that two groups of samples which are mutually exclusive, do not differ from each other in any way, i.e., have the same distribution.

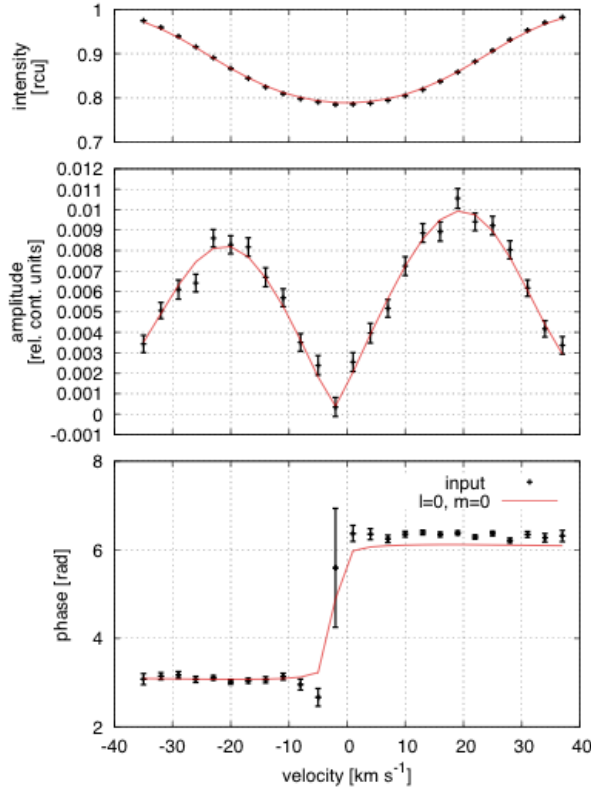


Figure 3.8: The Fourier parameters zero point, amplitude and phase (from top to bottom) of a radial mode in simulated data. The red line is a model plot for the values $(\ell, m) = (0, 0)$. From Zima (2005).

For N independent observations o_i , with a variance σ_i^2 and a theoretical fit f_i for each measurement, χ^2 is defined as

$$\chi^2 = \sum_{i=1}^N \left[\frac{(o_i - f_i)^2}{\sigma_i^2} \right]. \quad (3.22)$$

By normalizing χ^2 by the degrees of freedom $\nu = N - m$, m being the number of free parameters, one receives the reduced χ_ν^2 :

$$\chi_\nu^2 = \frac{\chi^2}{\nu}. \quad (3.23)$$

Whenever the null hypothesis is true, the result of the test will be $\chi_\nu^2 = 1$. For values of $\chi_\nu^2 < 1$, Equations 3.22 and 3.23 inevitably lead to $(o_i - f_i)^2 < \sigma_i^2$ or $(o_i - f_i)^2 < \nu$, respectively. Thus, the fit is better than the observational errors, which is not necessarily a better result. The application of the χ^2 -test to the FPF

method, using the complex amplitudes of the Fourier analysis, is done by Zima (2006) in the following way:

$$\chi_\nu^2 = \frac{1}{2n_\lambda - m} \sum_{i=1}^{n_\lambda} \left[\frac{(A_{R,i}^o - A_{R,i}^t)^2}{\sigma_{R,i}^2} + \frac{(A_{I,i}^o - A_{I,i}^t)^2}{\sigma_{I,i}^2} \right], \quad (3.24)$$

with n_λ being the number of pixels across the line and A^o , A^t denoting the observed and theoretical amplitude, respectively. The real part of the amplitude is written as $A_R = A_\lambda \cos \phi_\lambda$, while its imaginary part is $A_I = A_\lambda \sin \phi_\lambda$. σ^2 is the variance of the observations and can also be separated in a real and an imaginary part.

For pulsations with low amplitudes, the zero point Z_λ can be regarded as pulsationally independent. By assuming a non-pulsating star, a theoretical fit to the observed value Z_λ allows the determination of a series of parameters. The projected rotational velocity $v \sin i$, the intrinsic line width σ and the equivalent width EW describe the properties of the line profile, which are independent of the pulsations and, hence, equal for all pulsation modes.

3.2.3.2 Genetic optimization algorithm

In order to define the model that approximates the observed values best, a genetic optimization algorithm is applied. As the name implies, this method mimics the way the natural evolutionary selection process works, by favoring better adapted individuals.

A number of n starting individuals with stochastically selected properties is set as the first generation. The goodness-of-fit, i.e. the χ_ν^2 , which is calculated for each individual, decides whether or not it is eligible to pass on its genetic information. As soon as a group of parents is selected, their attributes, which are coded as a string of binary bits, are exchanged, in order to create new descendants. By randomly inverting single bits of individuals, mutations are created to ensure that the full parameter space is taken into account and to find the global minimum. The members of the new generation are then again tested for their fitness and used for another iteration of the algorithm. Once a satisfying minimum is found, or a certain number of generations is reached, the process of evolutionary selection and reproduction is stopped.

The parameters to be optimized lie within a certain interval, with a step size that can be defined before the algorithm is started. Also, the size of the population in one generation and the number of maximal iterations are set beforehand. These values largely affect the time in which a global minimum is reached. A more precise search of the parameter space and a higher number of individuals will result in longer computational times. Furthermore, it is necessary to perform a separate optimization for each combination of (ℓ, m) , since the estimation of discrete parameters proves to be very difficult (see Section 3.1.2).

Chapter 4

Results

4.1 The absorption lines

The absorption lines used for the analysis were proposed by Castanheira et al. (2008). As already explained in Section 3.2.1.1, the most important criterion for the selection of the lines is that they are unblended. Furthermore, they need to be deep, which is the case for the two FeII lines.

Since the first attempt at mode identification yielded very high χ^2 values for both lines, but especially for the line at 4549 Å, the lines were checked for their eligibility. A synthetic spectrum with a temperature of $T_{\text{eff}} = 6800$ K, and a surface gravity of $\log g = 3.2$ was calculated. When the synthetic spectrum is rotationally broadened by a projected rotational velocity of $v \sin i = 120 \text{ km s}^{-1}$, the line at 4508.288 Å becomes slightly blended at the wings (see Figure 4.1). This cannot be avoided, as for a star with such a high $v \sin i$ most lines are blended. Therefore, the line was selected for the analysis.

However, the line at 4549.474 Å is highly blended by TiII at 4549.617 Å, already at zero velocity (see Figure 4.2). Thus, this line was omitted for the mode identification. Since it is not so crucial for frequency analysis, whether the line is blended or not, the frequencies found for this line are still listed below. Also, they are in good agreement with the results of the analysis of the line at 4508 Å.

4.2 Frequency analysis

All results were obtained using the software FAMIAS (Zima, 2008).

Prior to the analysis, all spectra were checked thoroughly for flaws. Those with emissions due to cosmic rays or with very strong noise were deleted, since they are

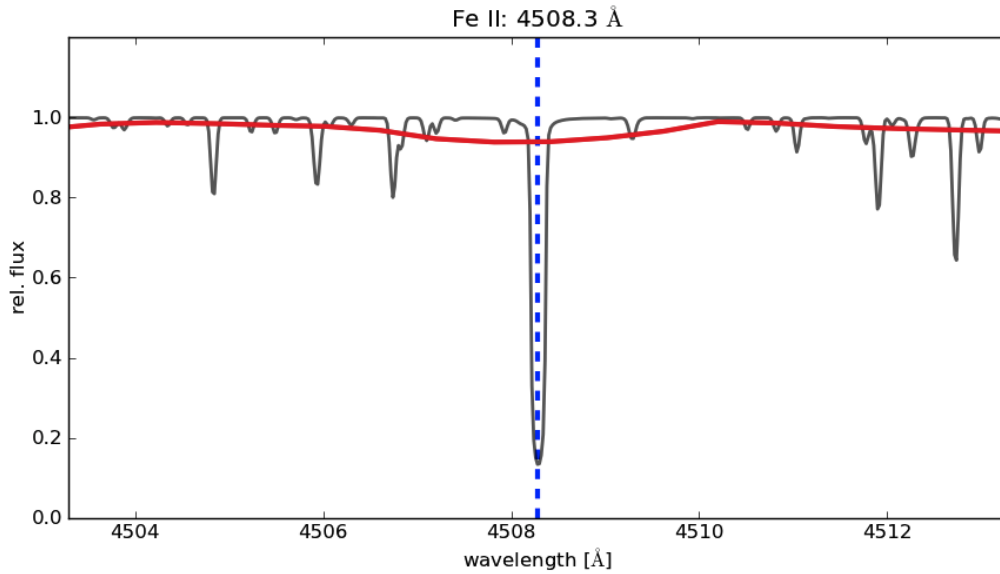


Figure 4.1: The black line represents the synthetic spectrum with the properties of $T_{\text{eff}} = 6800$ K, $\log g = 3.2$, and zero velocity. The rotationally broadened synthetic spectrum with a $v \sin i = 120 \text{ km s}^{-1}$ is represented by a red line. Indicated by the blue dashed line is the line center at 4508.288 \AA . Credits to Paul Beck.

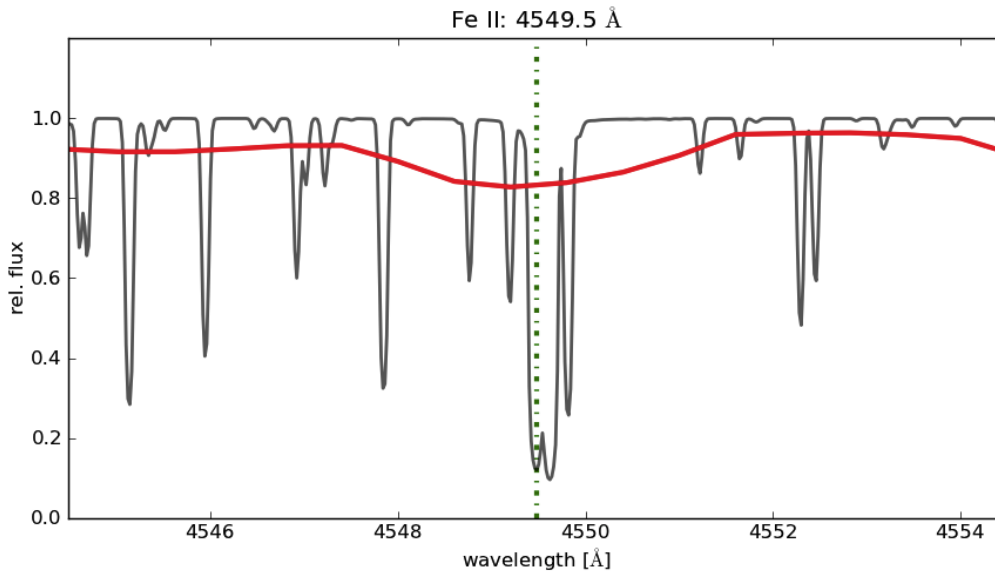


Figure 4.2: A synthetic spectrum with the same properties as the spectrum in Figure 4.1. The black line is the synthetic spectrum at zero velocity, while the red line is the synthetic spectrum rotationally broadened by a $v \sin i$ of 120 km s^{-1} . The line center at 4549.474 \AA is marked by the green dash-dotted line. Credits to Paul Beck.

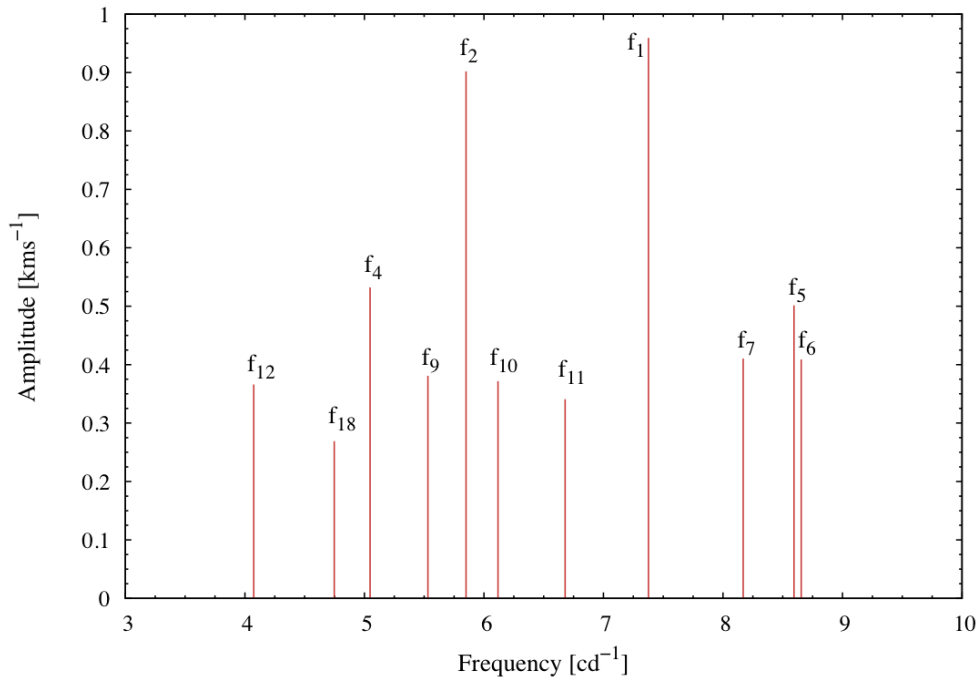


Figure 4.3: The frequencies of the line 4508 Å.

corrupt and unfeasible for our purpose. In total nine spectra were dropped. The remaining 758 measurements were weighted according to their S/N, whereas spectra of higher quality received a higher weight. Thus, the noise of the Fourier spectrum was kept low.

The frequency analysis was performed by means of a Fourier transform. After the periodogram was compared to the spectral window (see Fig. 3.5), the highest peaks were selected for a least-squares fitting to optimize the Fourier parameters and to calculate the S/N of each mode (see Section 3.1). Thereby, the deviations of amplitude and phase across the line are derived. The computed fit was then used to prewhiten the data. This process was iterated until the noise level in the amplitude spectrum was reached and no more significant frequencies could be found. Consequently, all frequency peaks with an amplitude S/N ratio < 4 were not included (Breger et al., 1993).

Figure 4.4 displays the amplitude spectrum of the original data (top panel) and four periodograms of prewhitened data. The strong one-day aliasing obscures most frequencies and the real peaks only become visible after the main periodicities are subtracted from the signal. The bottom panel of Fig. 4.4 shows the last obtained

4 Results

Table 4.1: Frequencies found in the two FeII lines 4508 Å and 4549 Å. The frequency resolution is 0.01 cd^{-1} and the average error in amplitude is 0.08 km s^{-1} and 0.1 km s^{-1} , respectively. The frequencies f_{13} and f_{18} are all $< 1.2 \text{ cd}^{-1}$. Those as well as f_3 and f_8 can be explained by the length of the data set, the different runs as well as longer gaps between the observations.

	Frequency [cd^{-1}]	Amp. 4508 Å [km s^{-1}]	Amp. 4549 Å [km s^{-1}]
f_1	7.38	0.96	2.1
f_2	5.85	0.90	2.4
f_4	5.04	0.53	1.3
f_5	8.59	0.50	1.6
f_6	8.65	0.41	0.8
f_7	8.17	0.41	0.7
f_9	5.53	0.38	0.9
f_{10}	6.12	0.37	0.8
f_{11}	6.68	0.34	0.7
f_{12}	4.07	0.37	0.7
f_{18}	4.75	0.27	0.7
f_3	0.0104	0.71	2.0
f_8	0.0603	0.4	-

Fourier spectrum. Although there seems to be still some periodicity left in the data, the noise level was already too high to find reliable frequency peaks. Figures 4.6 to 4.11 display the results of the least-squares fitting of all significant frequencies.

The intrinsic frequencies of the star are listed in Table 4.1 and are displayed graphically in Figure 4.3. The results are in good agreement with previous photometric studies (see Section 1.4). However, the frequencies $f_6 = 8.65 \text{ cd}^{-1}$, $f_7 = 8.17 \text{ cd}^{-1}$, and $f_{12} = 4.07 \text{ cd}^{-1}$ could only be detected in the spectroscopic data set.

The general increase in noise toward lower frequencies in Fig. 4.4 can be explained by the short length of the data set, which only spans over four months, and the long gaps between the different runs. As they allow periodicities of several days to be fitted to the data, many frequency peaks $< 1 \text{ cd}^{-1}$ occur. The most significant low-frequency peak is $f_3 = 0.0104 \text{ cd}^{-1}$, which is $\sim 1/T$, with $T = 96 \text{ d}$, resembling the length of the data set.

While the last detected frequency, $f_{18} = 4.75$ already has an amplitude below the significance limit in the data set of the line 4508 Å, it has a higher S/N in the

Table 4.2: The pulsational independent parameters.

$v \sin i$	$105.3 \pm 0.7 \text{ kms}^{-1}$
EW	$15.12 \pm 0.01 \text{ kms}^{-1}$
σ	$8.9 \pm 0.4 \text{ kms}^{-1}$
dZ	$-21.59 \pm 0.04 \text{ kms}^{-1}$

data set of the line 4549 \AA and was already confirmed by photometry (Breger et al., 1999; Breger, 2000b). For these reasons, a mode identification was performed for this frequency as well. The results, however, should be treated with caution.

4.3 Mode identification

The mode identification was carried out by means of the Fourier parameter fit method (see Section 3.2.3), implemented in FAMIAS (Zima, 2008). Thereby, theoretical models are fitted to the amplitude across the line and phase across the line. A χ^2 -test was then applied to derive the significance of the fit.

First, the zero point profile (see Figure 4.5), which is identical for every pulsation mode, is fitted with a non-rotating model to derive starting values for the pulsational independent parameters. These are the inclination i , the projected rotational velocity $v \sin i$, the equivalent width EW , the intrinsic width σ and the zero point offset dZ . Since the pulsations still contribute to the width of the zero point, these parameters were kept variable for the fitting of amplitude and phase of each mode.

The intervals within which the free parameters were calculated, were narrowed in an iterative process until they were within an acceptable error range (see Table 4.2). While the limits and step rate of the pulsational independent values were equal for each mode in every iteration, the interval of the line-profile parameters were defined for each mode separately.

A definite value for EW and dZ could already be determined after a few iterations. Thus, they were kept constant for all further calculations. However, the scatter of i , $v \sin i$, and σ was much larger. The values of $v \sin i$ and σ could only be calculated within a slightly larger error range than EW and dZ , and were set to constant values for the last iteration.

Tables 4.3 to 4.5 display the five to eight best combinations of (ℓ, m) with the pulsational velocity v_p , i , $v \sin i$, and σ set as free parameters. The results of the

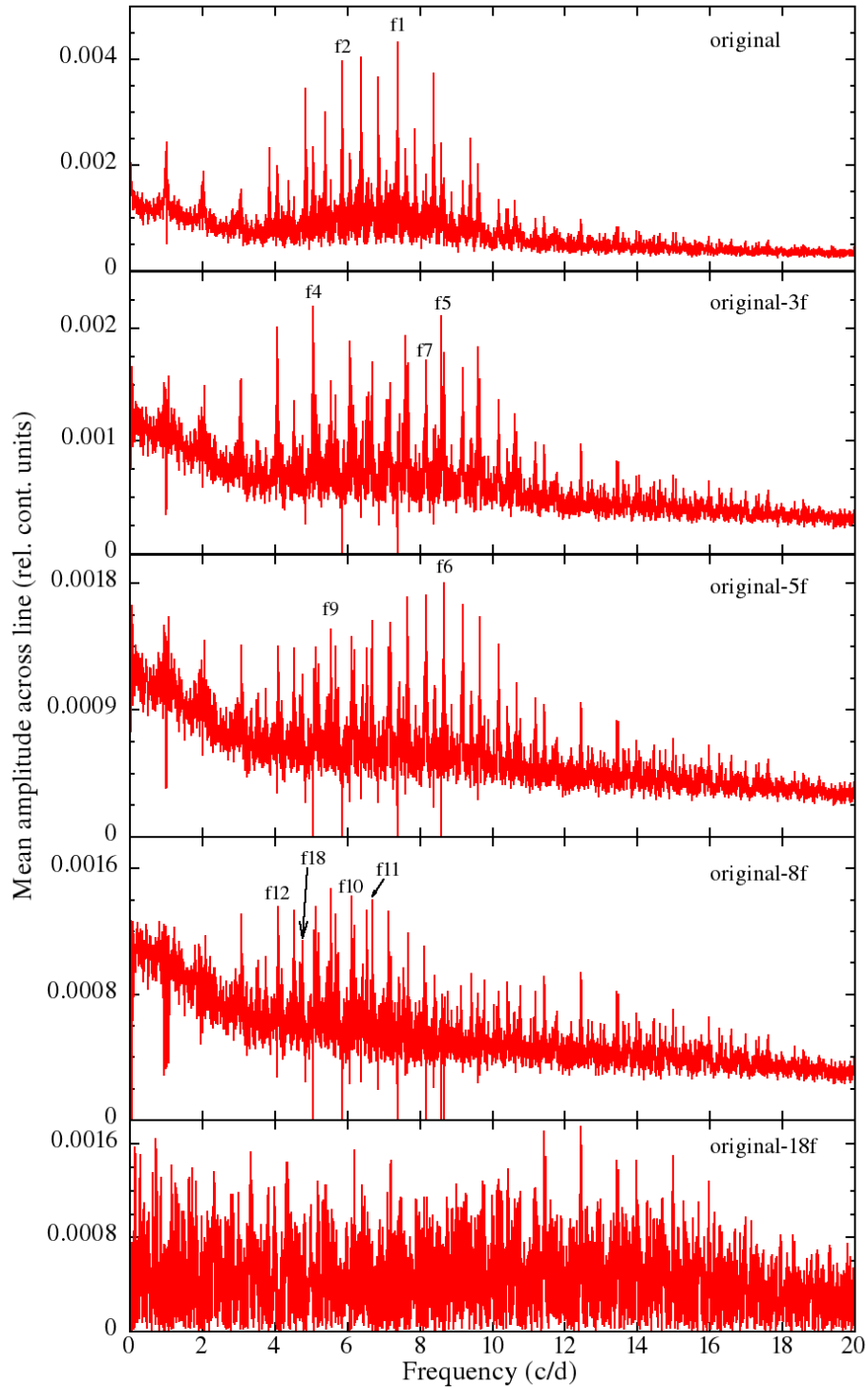


Figure 4.4: One-dimensional Fourier spectra of the wavelength-bin variations. The amplitude is the mean amplitude across the line per frequency with a unit relative to the continuum level. Each panel displays a periodogram prewhitened by the frequencies indicated in the right top. Note that the amplitude scale changes from top to bottom.

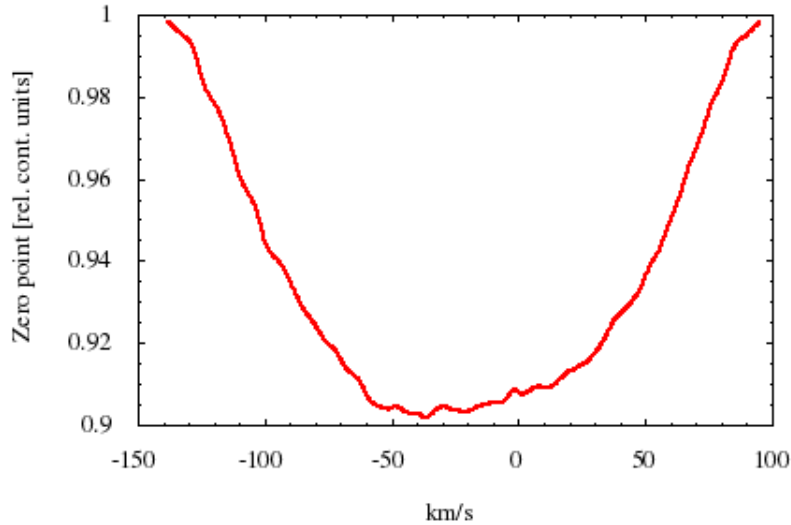


Figure 4.5: The zero-point profile of the line 4508 Å.

calculations with $v \sin i$, EW , σ , and dZ set to constant values, are listed in Table 4.6. Only the models with the lowest χ_ν^2 value are shown. The slight increase in χ_ν^2 compared to the previous results can be explained by the uncertainty of the derived $v \sin i$ and σ .

On the other hand, it was not possible to derive the inclination i . Although most of the displayed results tend to favor a higher inclination from $\sim 66^\circ$ to $\sim 88^\circ$, the many outliers and the strong scatter prevented a clear determination of the value of i .

The mode parameters can be determined by fitting the amplitude and phase across the line (displayed in Figs. 4.6 to 4.11). Whereas the phase is especially sensitive to the azimuthal order m , the degree ℓ is defined by the amplitude. However, ℓ values derived by means of multicolor photometry are more reliable than the results obtained by an analysis of the line-profile variations. On the other hand, the spectroscopic mode identification is much more suitable to determine the value of m .

Positive gradients in phase (see right panel of Fig. 4.6, f_1 for an example) result in negative values of m , thus it is a retrograde mode. On the other hand, a negative gradient in phase (for example the phase of f_2 , see left panel of Fig. 4.6) means a positive value for m and therefore a prograde mode. A not uniformly continuous gradient indicates an axisymmetric mode ($m = 0$). For the modes $f_4 = 5.05 \text{ cd}^{-1}$, $f_{10} = 6.12 \text{ cd}^{-1}$, $f_{12} = 4.07 \text{ cd}^{-1}$, and $f_{18} = 4.75 \text{ cd}^{-1}$ this case cannot be ruled out.

4 Results

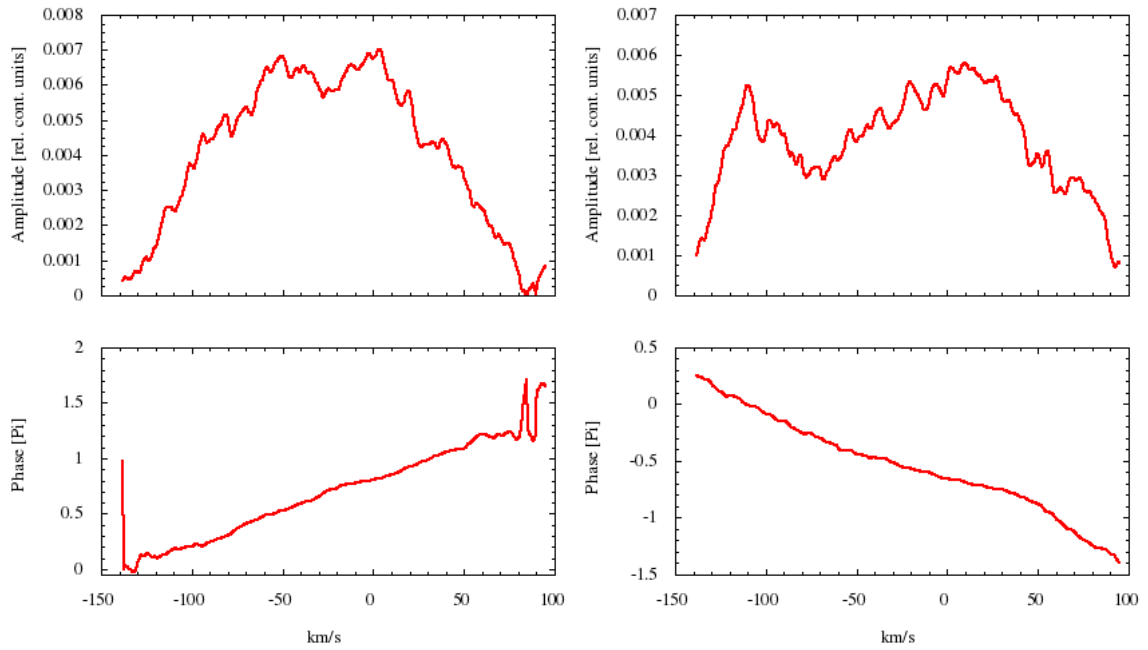


Figure 4.6: The amplitude and phase across the line of $f_1 = 7.38 \text{ cd}^{-1}$ (left panel) and $f_2 = 5.85 \text{ cd}^{-1}$ (right panel), derived by means of a least-squares fit of all significant frequencies.

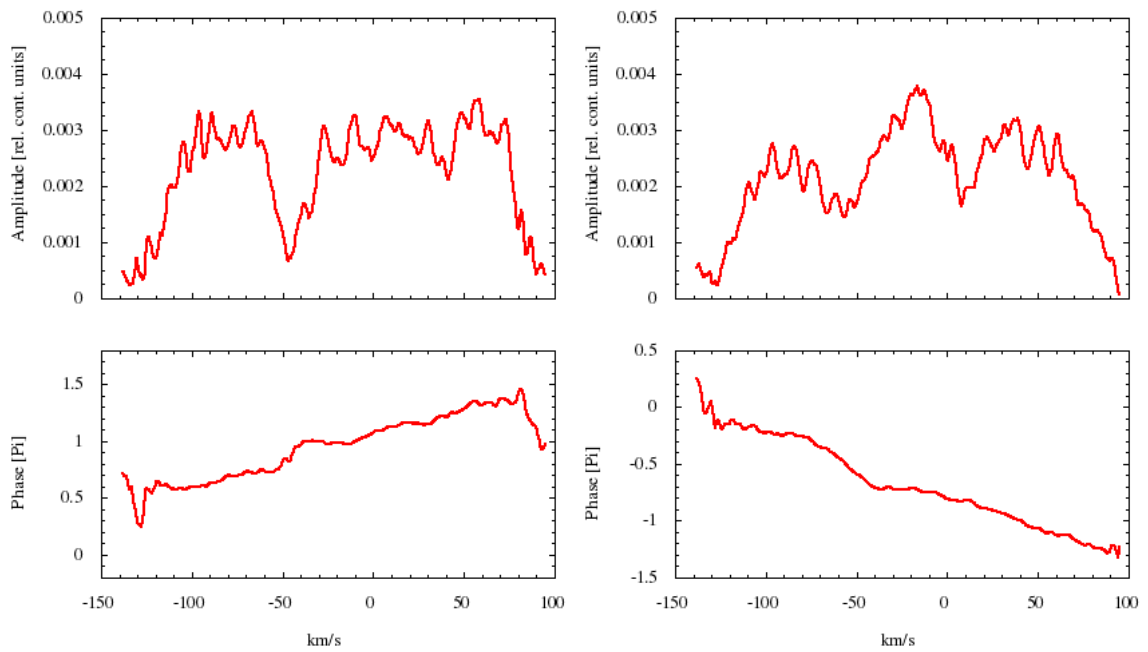


Figure 4.7: The amplitude and phase across the line of $f_4 = 5.05 \text{ cd}^{-1}$ (left panel) and $f_5 = 8.59 \text{ cd}^{-1}$ (right panel).

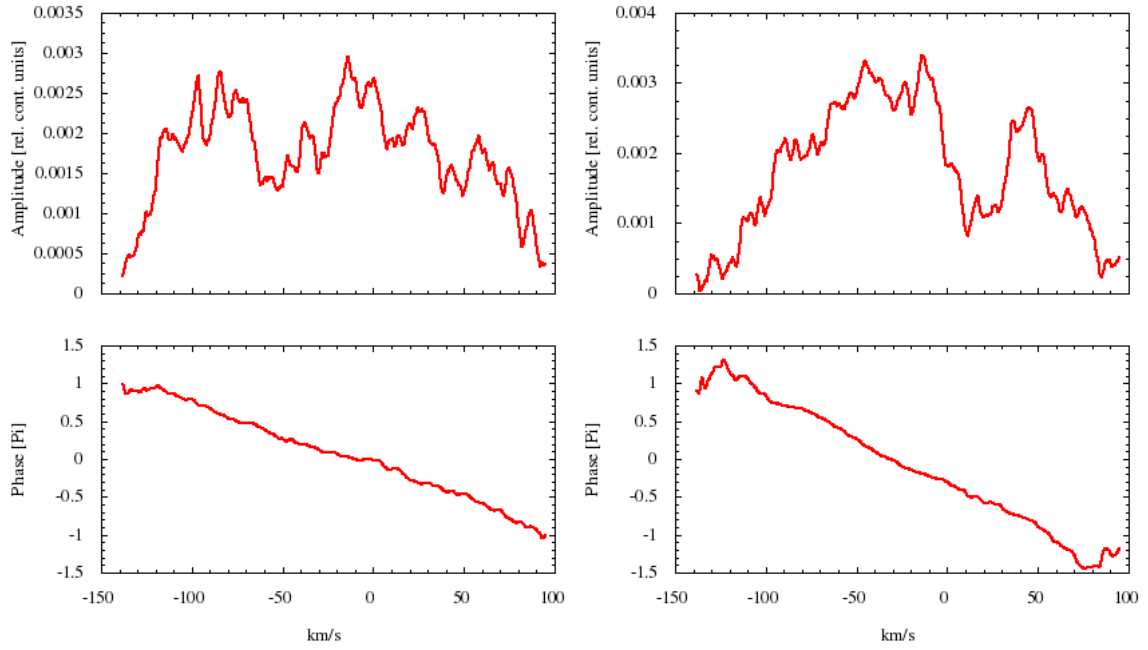


Figure 4.8: The amplitude and phase across the line of $f_6 = 8.65 \text{ cd}^{-1}$ (left panel) and $f_7 = 8.17 \text{ cd}^{-1}$ (right panel).

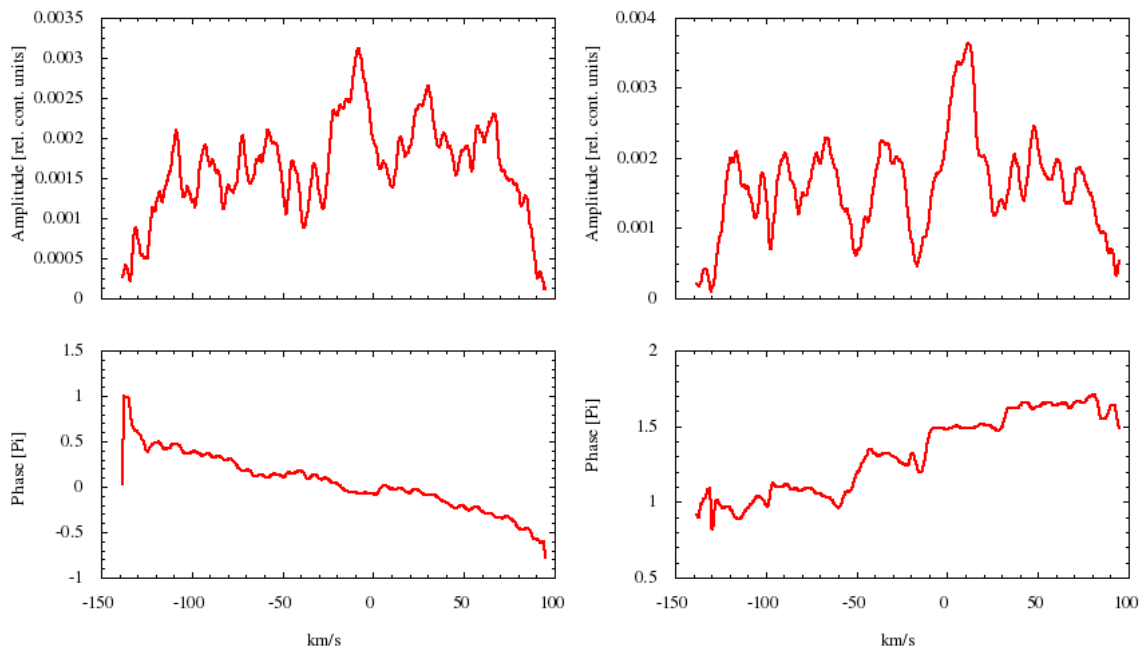


Figure 4.9: The amplitude and phase across the line of $f_9 = 5.53 \text{ cd}^{-1}$ (left panel) and $f_{10} = 6.12 \text{ cd}^{-1}$ (right panel).

4 Results

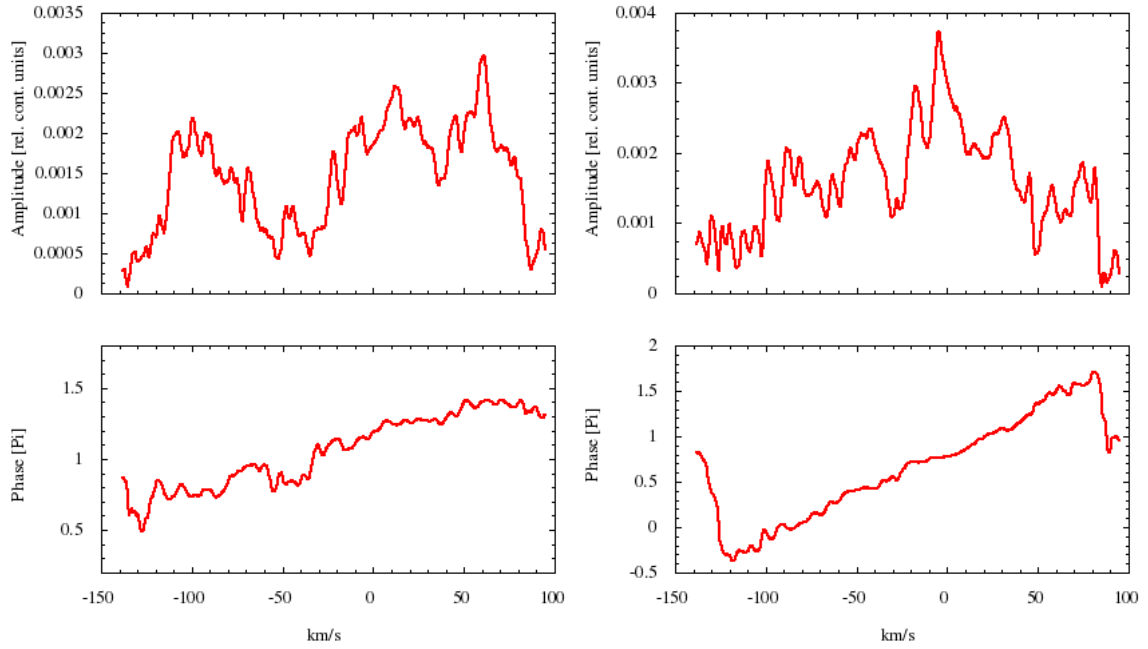


Figure 4.10: The amplitude and phase across the line of $f_{11} = 6.68 \text{ cd}^{-1}$ (left panel) and $f_{12} = 4.07 \text{ cd}^{-1}$ (right panel).

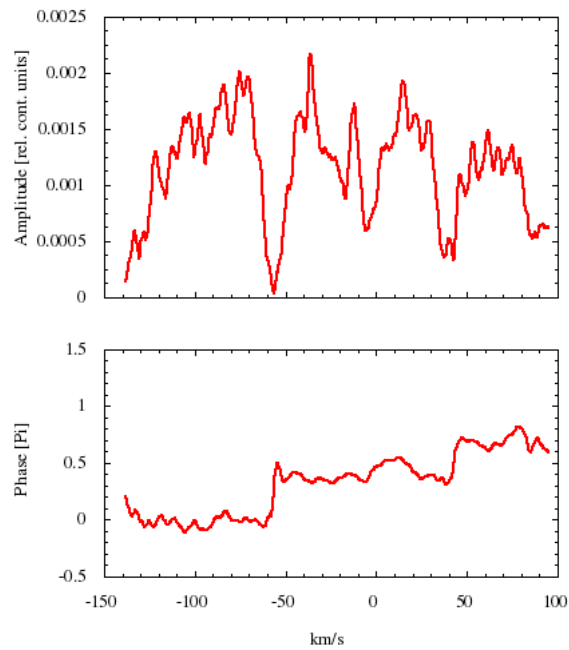


Figure 4.11: The amplitude and phase across the line of $f_{18} = 4.75 \text{ cd}^{-1}$.

Table 4.3: The best combinations of (ℓ, m) and the best values for the mode parameters are listed for each mode. The velocity amplitude v_p , the projected rotational velocity $v \sin i$, and the intrinsic width σ are in units of kms^{-1} , while the inclination angle i is expressed in degrees. All results were derived by means of the FPF method. While $v \sin i$, σ , and i are set as free parameters, the other pulsational independent quantities EW and dZ were set to the constant values 15.12kms^{-1} and -21.59kms^{-1} , respectively.

$f_1 = 7.38 \text{ cd}^{-1}$						
χ_ν^2	ℓ	m	v_p	i	$v \sin i$	σ
19.57	3	-1	44.29	56.7	104.6	9.2
26.06	3	-3	10.28	53.8	105.9	8.8
26.68	3	-2	10.98	37.6	105.8	8.7
31.73	2	-2	15.94	34.8	105.7	8.8
38.45	2	-1	11.34	30	105.7	8.7
$f_2 = 5.85 \text{ cd}^{-1}$						
χ_ν^2	ℓ	m	v_p	i	$v \sin i$	σ
35.16	3	2	0.48	31.9	105.5	9.3
46.67	3	1	2.38	35.7	105.8	8.5
56.81	2	2	0.95	30	105.8	8.7
59.86	2	1	5.24	71.9	105.7	8.9
60.23	3	3	0.48	42.4	105.6	9.4
$f_4 = 5.05 \text{ cd}^{-1}$						
χ_ν^2	ℓ	m	v_p	i	$v \sin i$	σ
14.09	2	-1	61.49	87.1	104.3	8.9
18.08	3	0	24.98	84.3	104.7	9.4
22.44	2	0	8.51	67.1	105.9	8.7
22.54	1	-1	10.43	39.5	105.9	8.7
23.09	3	-2	33.76	86.2	105.3	8.5
$f_5 = 8.59 \text{ cd}^{-1}$						
χ_ν^2	ℓ	m	v_p	i	$v \sin i$	σ
23.76	3	1	7.29	51	105.9	8.7
23.96	3	2	4.59	71	105.9	8.6
26.46	2	2	3.24	89	105.9	8.6
27.13	2	1	14.71	81.4	105.9	8.5
27.34	1	1	6.53	39.5	105.9	8.6

Table 4.4: Table 4.3 continued.

$f_6 = 8.65 \text{ cd}^{-1}$						
χ_ν^2	ℓ	m	v_p	i	$v \sin i$	σ
15.50	8	1	25.51	81.4	104.8	9.2
16.78	9	2	19.21	80.5	104.8	9
19.05	10	2	15.75	73.8	105.1	9
19.67	10	1	20.47	83.3	104.8	9.4
20.01	8	2	19.53	75.7	105	9.1
20.20	9	1	21.73	71.9	105.1	9.1
20.55	7	1	26.14	74.8	105	9.2
20.80	6	1	34.65	86.2	104.5	9.1
$f_7 = 8.17 \text{ cd}^{-1}$						
χ_ν^2	ℓ	m	v_p	i	$v \sin i$	σ
17.37	12	3	7.45	77.6	105.3	8.5
17.46	11	2	11.18	78.6	105.3	8.6
17.55	11	3	8.04	78.6	105.3	8.4
17.67	10	1	16.18	80.5	105.1	8.9
17.92	10	2	11.86	79.5	105.3	8.7
18.39	9	1	17.25	82.4	105.1	9.4
18.53	12	2	9.22	72.9	105.5	8.5
19.5	12	1	13.24	76.7	105.3	8.9
$f_9 = 5.53 \text{ cd}^{-1}$						
χ_ν^2	ℓ	m	v_p	i	$v \sin i$	σ
21.34	3	2	1.07	66.2	106	8.6
22.18	3	1	1.13	37.6	106	8.6
22.40	2	1	1.64	45.2	105.9	8.6
24.26	2	2	0.38	31	106	8.7
25.16	1	1	2.33	81.4	106	8.6

Table 4.5: Table 4.4 continued.

$f_{10} = 6.12 \text{ cd}^{-1}$						
χ_ν^2	ℓ	m	v_p	i	$v \sin i$	σ
15.90	3	0	34.71	86.2	104.5	9.4
17.22	2	-1	38.0	87.1	105.3	8.9
21.24	1	-1	5.09	57.6	106	8.5
21.47	2	0	7.78	66.2	105.9	8.6
21.54	3	-2	37.7	88.1	105	8.7
$f_{11} = 6.68 \text{ cd}^{-1}$						
χ_ν^2	ℓ	m	v_p	i	$v \sin i$	σ
14.54	2	-1	66.35	88.1	104.3	9.4
20.33	1	-1	4.94	66.2	106	8.6
21.57	2	-2	3.18	84.3	106	8.6
21.78	3	-1	5.29	44.3	106	8.6
22.62	3	-2	5.65	75.7	105.9	8.6
$f_{12} = 4.07 \text{ cd}^{-1}$						
14.98	7	0	7.56	84.3	105	9.3
15.02	8	-1	11.65	81.4	104.9	9.4
15.86	5	0	9.45	86.2	105.1	9.2
16.58	6	-1	15.12	83.3	104.9	9.4
18.56	7	-2	24.57	85.2	104.3	9.3
18.74	5	-2	34.33	86.2	104.3	8.5
19.88	5	-1	10.39	71	105.6	9.2
$f_{18} = 4.75 \text{ cd}^{-1}$						
χ_ν^2	ℓ	m	v_p	i	$v \sin i$	σ
12.67	2	-1	59.65	89	104.4	8.7
14.57	3	0	20.9	87.1	104.8	9.4
20.53	1	-1	5.1	33.8	106	8.6
20.88	3	-1	3.82	88.1	106	8.6
20.90	2	-2	2.8	59.5	106	8.5

Table 4.6: The models with the lowest χ_ν^2 value are listed for each mode. The pulsational independent parameters were set as the constant values, which are mentioned in Table 4.2. Since $v \sin i$ and σ are not set as free parameters, the χ_ν^2 values are slightly higher than the respective results in Tables 4.3 to 4.5.

	Frequency [cd ⁻¹]	χ_ν^2	ℓ	m	v_p [kms ⁻¹]	i
f_1	7.38	20.63	3	-1	37.48	55.7
f_2	5.85	36.85	3	2	0.47	31.9
f_4	5.05	15.97	2	-1	48.59	86.2
f_5	8.59	24.73	3	1	7.39	50
f_6	8.65	15.95	8	1	23.62	81.4
f_7	8.17	17.50	11	2	10.9	78.6
f_9	5.53	22.72	3	2	1.32	70
f_{10}	6.12	16.87	2	-1	40.0	87.1
f_{11}	6.68	17.01	2	-1	53.33	88.1
f_{12}	4.07	15.08	7	0	7.24	84.3
f_{18}	4.75	14.05	2	-1	47.16	88.1

Figs. 4.7 (left panel), 4.9 (right panel), 4.10 (right panel), and 4.11 clearly show smaller to larger bumps in the phase plot, which could have influenced the results. Moreover, the derived m values are in good agreement with the findings for the phase variations of the modes by Breger (2010).

The amplitude across the line of each mode shows a large scatter from pixel to pixel. This leads to larger deviations between the model fit and the measurements, which could explain the generally high χ_ν^2 values. In addition, the poorly fitted amplitude causes an overestimation of the degree ℓ . The ℓ values, which were determined using multicolor photometry (see Table 1.1), lie all below the spectroscopic results. Since this method is more sensitive to the degree of the mode, the photometric results should be favored.

Those frequencies which were not detected in the photometric data could be assigned with an $\ell > 4$. Partial cancellation effects lead to small amplitudes for high-degree modes in photometric light curves, which measure the total brightness integrated over the stellar disc (see Section 1.1.2). Therefore, the high ℓ values derived for the modes $f_6 = 8.65 \text{ cd}^{-1}$, $f_7 = 8.17 \text{ cd}^{-1}$ and $f_{12} = 4.07 \text{ cd}^{-1}$ are compatible with the current theory of non-radial pulsations.

Chapter 5

Conclusion

In this thesis I present the results of the analysis of the spectroscopic measurements of the δ Scuti star 4 CVn obtained at McDonald Observatory (Davis Mountains in West Texas, USA) in the year 2010. The reduction process of the highly resolved stellar spectra was improved by introducing a correction for the instrumental blaze function. Also, the manual continuum normalization conducted with a special IRAF task was omitted in favor of an automated procedure. This procedure was carried out with a Python script specifically coded for the purpose of this research and aimed at raising the wings of the selected lines to a uniform value. Since the star is a very fast rotator ($v \sin i = 105.3 \text{ km s}^{-1}$), the absorption lines are heavily broadened and there is nearly no continuum visible in the spectra. Thus, the normalization of the line wings led to much better results than the fitting of the shape of the orders with the IRAF task `continuum`. All further analysis of the line-profile variations were performed with the software FAMIAS.

After a thorough inspection of every measurement, the line moments were calculated to investigate the properties of the line. The non-sinusoidal shifts in the first moment, which represents radial velocity, led to the discovery, that the star is a single-lined binary with an excentric orbit with a period of 124.3 d. This trend was corrected with a Keplerian orbit-fit.

Subsequently, the variations of the profiles of two FeII absorption lines at 4508.288 Å and 4549.474 Å were studied by means of the pixel-by-pixel method. Unfortunately, in the course of the research the second line turned out to be highly blended with the TiII line at 4549.617 Å, and thus it proved unsuitable for the attempted methods.

The first step of the analysis involved a Fourier analysis of the temporal variations of each wavelength bin of the line profile to search for frequencies in the data set.

The amplitude and the phase across the line was then obtained by means of a least-squares fitting. These Fourier parameters were then fitted with theoretical values derived from the analysis of synthetic line profiles. By these means, it was possible to determine the parameters of the line profile and the properties of the mode.

The applied methods, i.e., the Fourier analysis, the least-squares algorithm, the moment method, the pixel-by-pixel method and its advancement, the Fourier parameter fit method, as well as the theory of the line-profile variations were studied in detail and are elaborately explained in this thesis.

The evaluation led to the detection of many pulsation modes, most of which were already discovered in photometry. However, three of the frequencies could only be found in the spectroscopic data set. The subsequent mode identification yielded high ℓ values for these modes. This result is not surprising, since partial cancellation effects aggravate the detection of high-degree modes in photometry. Furthermore, I was able to assign values of ℓ and m to the assumed intrinsic frequencies of the star. Also, the line parameters and the projected rotational velocity $v \sin i$ could be derived. The new value of $v \sin i = 105.3 \pm 0.7 \text{ km s}^{-1}$ is slightly lower than the previously determined with $v \sin i > 120 \text{ km s}^{-1}$ (Castanheira et al., 2008).

The results for the azimuthal order m are in especially good agreement with the results of Castanheira et al. (2008) and of Breger (2010), as far as the phase variations of retrograde and prograde modes are concerned. On the other hand, the degrees of the modes derived during my research are slightly higher compared to previous photometric results and those of Castanheira et al. (2008). Also, I could only obtain high χ^2_ν values > 10 for the calculated models, indicating that none of the results have a high significance.

The deviations between the results presented here and the outcome of the analysis of the data set in 2008 originate from a slightly different approach chosen by Castanheira et al. (2008). For instance, the reduction process was altered compared to Castanheira et al. (2008), as they performed a manual continuum normalization. Secondly, the new discovery of the binary system allowed the correction of the drift in radial velocity due to the orbital motion, which was not detected by Castanheira et al. (2008). Furthermore, they used the highly blended FeII line at 4549 Å and combined it with the nearly unblended line at 4508 Å to improve the S/N. The results published by Castanheira et al. (2008) are derived from the analysis of the combined line-profile variations.

However, the origin of the high χ^2_ν values still need to be investigated. One reason could be the large scatter of the amplitudes across the line for each mode which leads to large discrepancies between the model fit and the measurements. An attempt to remedy this situation could be to find other unblended lines in the spectra and rerun the analysis. Also, the combination of several unblended metal absorption lines could help to improve the S/N and thus minimize the noise of the spectra.

The star 4 CVn is one of the most detailed studied δ Scuti stars (Breger et al., 1999; Breger, 2000b; Breger et al., 2008; Breger, 2010) with photometric light curves obtained over several decades and three years worth of highly resolved time-series spectroscopy. Thus, a modification of the analysis of the spectroscopic line-profile variations of all the three years, 2008, 2010, and 2011 would be a suitable topic of further investigations. More accurate mode identification could serve as a good input for seismic modeling and in this way help gain promising new insights in the field of asteroseismology.

Bibliography

- Aerts, C., Christensen-Dalsgaard, J., and Kurtz, D. W. (2010). *Asteroseismology*. Springer.
- Aerts, C., de Pauw, M., and Waelkens, C. (1992). Mode identification of pulsating stars from line profile variations with the moment method. an example - The Beta Cephei star Delta Ceti. *Astron. & Astrophys.*, 266:294–306.
- Breger, M. (2000a). δ Scuti stars (Review). In Breger, M. and Montgomery, M., editors, *Delta Scuti and Related Stars*, volume 210 of *Astronomical Society of the Pacific Conference Series*, page 3.
- Breger, M. (2000b). The multiperiodic δ Scuti star 4 Canum Venaticorum: amplitude variability. *Mon. Not. R. Astron. Soc.*, 313:129–135.
- Breger, M. (2010). The Blazhko Effect in Delta Scuti and Other Groups of Pulsating Stars. In Sterken, C., Samus, N., and Szabados, L., editors, *Variable Stars, the Galactic halo and Galaxy Formation*, page 95.
- Breger, M., Davis, K. A., and Dukes, R. J. (2008). The amplitudes of the δ Scuti star 4 CVn in 1991. *Communications in Asteroseismology*, 153:63–66.
- Breger, M., Handler, G., Garrido, R., Audard, N., Zima, W., Páparó, M., Beichbuechner, F., Li, Z.-P., Jiang, S.-Y., Liu, Z.-L., Zhou, A.-Y., Pikall, H., Stankov, A., Guzik, J. A., Sperl, M., Krzesinski, J., Ogloza, W., Pajdosz, G., Zola, S., Thomassen, T., Solheim, J.-E., Serkowitsch, E., Reegen, P., Rumpf, T., Schmalwieser, A., and Montgomery, M. H. (1999). 30+ frequencies for the delta Scuti variable 4 Canum Venaticorum: results of the 1996 multisite campaign. *Astron. & Astrophys.*, 349:225–235.
- Breger, M., Stich, J., Garrido, R., Martin, B., Jiang, S. Y., Li, Z. P., Hube, D. P., Ostermann, W., Páparo, M., and Scheck, M. (1993). Nonradial Pulsation of

- the Delta-Scuti Star Bu-Cancri in the Praesepe Cluster. *Astron. & Astrophys.*, 271:482.
- Castanheira, B. G., Breger, M., Beck, P. G., Elmasli, A., Lenz, P., and Falcon, R. E. (2008). Spectroscopic mode identification of the δ Scuti star 4 CVn. *Communications in Asteroseismology*, 157:124–127.
- Collins, G. W. (1989). *The fundamentals of stellar astrophysics*.
- Cunha, M. S., Aerts, C., Christensen-Dalsgaard, J., Baglin, A., Bigot, L., Brown, T. M., Catala, C., Creevey, O. L., Domiciano de Souza, A., Eggenberger, P., Garcia, P. J. V., Grundahl, F., Kervella, P., Kurtz, D. W., Mathias, P., Miglio, A., Monteiro, M. J. P. F. G., Perrin, G., Pijpers, F. P., Pourbaix, D., Quirrenbach, A., Rousselet-Perraut, K., Teixeira, T. C., Thévenin, F., and Thompson, M. J. (2007). Asteroseismology and interferometry. *Astron. Astrophys. Rev.*, 14:217–360.
- de Pauw, M., Aerts, C., and Waelkens, C. (1993). Mode identification of pulsating stars from line profile variations with the moment method. A theoretical study of the accuracy of the method. *Astron. & Astrophys.*, 280:493–507.
- De Ridder, J., Dupret, M.-A., Neuforge, C., and Aerts, C. (2002). Influence of non-adiabatic temperature variations on line profile variations of slowly rotating beta Cephei stars and SPBs. II. Simulations of line profile time series. *Astron. & Astrophys.*, 385:572–584.
- Deeming, T. J. (1975). Fourier Analysis with Unequally-Spaced Data. *Astrophys. Space Sci.*, 36:137–158.
- Jeffrey, E. and Castanheira, B. G. (2010). *Sandiford Cassegrain Echelle Spectrograph (2.1m) Reduction Notes*.
- Kuschnig, R., Weiss, W. W., Gruber, R., Bely, P. Y., and Jenkner, H. (1997). Microvariability survey with the Hubble Space Telescope Fine Guidance Sensors. Exploring the instrumental properties. *Astron. & Astrophys.*, 328:544–550.
- Mathias, P., Gillet, D., Aerts, C., and Breitfellner, M. G. (1997). A spectroscopic study of the delta Scuti star rho Puppis. *Astron. & Astrophys.*, 327:1077–1086.
- McCarthy, J. K., Sandiford, B. A., Boyd, D., and Booth, J. (1993). The Sandiford 2.1-m Cassegrain echelle spectrograph for McDonald Observatory - Optical and mechanical design and performance. *Publ. Astron. Soc. Pac.*, 105:881–893.

BIBLIOGRAPHY

- Zima, W. (2005). *A New Spectroscopic Mode Identification Method and its Application to the δ Scuti Star FG Vir*. PhD thesis, University of Vienna, Austria.
- Zima, W. (2006). A new method for the spectroscopic identification of stellar non-radial pulsation modes. I. The method and numerical tests. *Astron. & Astrophys.*, 455:227–234.
- Zima, W. (2008). FAMIAS User Manual. *Communications in Asteroseismology*, 155:17–121.
- Zima, W., Wright, D., Bentley, J., Cottrell, P. L., Heiter, U., Mathias, P., Poretti, E., Lehmann, H., Montemayor, T. J., and Breger, M. (2006). A new method for the spectroscopic identification of stellar non-radial pulsation modes. II. Mode identification of the δ Scuti star FG Virginis. *Astron. & Astrophys.*, 455:235–246.

Danksagung

Zu allererst möchte ich meinen Eltern **Anna Schmid** und **Christian Schmid**, für die großartige Unterstützung in finanzieller und mentaler Hinsicht, großen Dank aussprechen. Ohne sie wäre es mir nicht möglich gewesen, so ungehindert zu studieren.

Auch meinem Diplombetreuer **Michel Breger** gebührt großer Dank. Er ermöglichte mir schon in einer sehr frühen Phase meines Studiums praktische Erfahrung in der täglichen Arbeit eines Astronomen zu sammeln. Von den Auslandsaufenthalten konnte ich auch persönlich sehr profitieren.

Bei **Conny Aerts** möchte ich mich für die tatkräftige Unterstützung während meines Ersasmusaufenthalts in Leuven bedanken. Sie hat trotz ihres vollen Terminkalenders immer noch Zeit für mich gefunden und ist mir auch nach Beendigung meiner Zeit in Leuven noch eine große Hilfe gewesen. Durch sie sind mir viele Türen in der akademischen Welt geöffnet worden.

Ein großes “Dankeschön” geht auch an **Veronique Fritz**, **Sabine Karrer**, **Nathalie Themessl** und **Stefan Meingast** die nicht nur sehr geschätzte Kollegen waren, sondern immer noch sehr gute Freunde sind, von denen ich viel gelernt hab. Ohne euch hätte das Studium nicht soviel Spaß gemacht!

Weiters möchte ich mich bei **Paul Beck** dafür bedanken, dass er mir während meines Aufenthaltes in Leuven mit Rat und Tat zur Seite gestanden ist. Er hat sich als sehr guter Kollege erwiesen und ich freue mich schon auf eine fruchtbare Zusammenarbeit in den kommenden Jahren.

Dank gebührt auch **Wolfgang Zima**, für die Einführung in FAMIAS, **Peter Papis**, für die Zuverfügungstellung seiner Programmierkenntnisse, **Vichi Antoci**, für die Hilfestellung bei der Datenreduktion und anderen fachlichen Fragen und

DANKSAGUNG

Jonas Debosscher für die Berechnung der Doppelsternmodelle.

Zu Dank bin ich auch **Barbara Castanheira** verpflichtet, die mich das Beobachten gelehrt hat und mir während meines Aufenthaltes in Texas zur Seite stand.

Zu guter Letzt möchte ich mich bei **Isolde Müller** dafür bedanken, dass sie sich die Zeit genommen hat, meine Arbeit korrekturzulesen.

Curriculum Vitae

Valentina Schmid

Geboren: 25.07.1987, Wien

Ausbildung

10. – 15. Sept. 2012	Sommer Schule „Binary Stars“ KU Leuven, Instituut voor Sterrenkunde Celestijnenlaan 200D, 3001 Leuven, Belgien
Sept. 2012	Abschluss des Masterstudiums Titel der Masterarbeit: „ <i>Spectroscopic Mode Identification of the Delta Scuti Star 4 CVn</i> “
2010 – 2012	Masterstudium Astronomie Universität Wien, Institut für Astronomie Türkenschanzstraße 17, 1180 Wien
Sept. 2011 – Febr. 2012	Erasmusaufenthalt KU Leuven, Instituut voor Sterrenkunde Celestijnenlaan 200D, 3001 Leuven, Belgien
29. Okt. 2010	Abschluss mit Auszeichnung Titel der Bakkalaureatsarbeit: „ <i>Einführung in die Theorie der Braunen Zwerge</i> “
2006 – 2010	Bakkalaureatsstudium Astronomie Universität Wien, Institut für Astronomie Türkenschanzstraße 17, 1180 Wien
Febr. 2010 – Apr. 2010	Auslandsaufenthalt an der University of Texas at Austin 2515 Speedway, Stop C1400 Austin, Texas 78712-1205, USA
12. Juni 2006	Abschluss mit Matura
2001 – 2006	HTBLVA, Höhere Lehranstalt für Elektronische Datenverarbeitung und Organisation Ausbildungsschwerpunkt: <i>Medientechnik und Medienwirtschaft</i> Spengergasse 20, 1050 Wien
1997 – 2001	BRG XIX, Allgemeinbildende Höhere Schule, Krottenbachstraße 11-13, 1190 Wien

Berufliche Laufbahn

2006 – 2012	Programmiererin mv edv Mühlgasse 1 / Objekt 8, 2353 Guntramsdorf
2009 – 2011	Wissenschaftliche Projektmitarbeiterin Projekt „ <i>Stellare Einblicke</i> “, Leitung: Prof. Dr. Michel Breger
März – Juni 2011	Tutorin für das <i>Astronomische Anfängerpraktikum</i> im 4. Semester Bakkalaureatsstudium Astronomie
März – Juni 2010	Tutorin für das <i>Astronomische Anfängerpraktikum</i> im 4. Semester Bakkalaureatsstudium Astronomie
Okt. 2009 – Jan. 2010	Tutorin für die <i>Einführung in die Astronomie I</i> im 1. Semester Bakkalaureatsstudium Astronomie

Beobachtungsaufenthalte

Okt. – Nov. 2011	Beobachtung am Mercator Teleskop am Observatorio del Roque de los Muchachos, La Palma, Spanien
18. Febr. – 05. März 2010 25. März – 09. Apr. 2010	Beobachtung am 2.1 m Otto-Struve-Teleskop am McDonald Observatory, Texas, USA

Konferenzen

20. – 25. Mai, 2012	ESF Konferenz „ <i>The Modern Era of Helio and Asteroseismology</i> “, mit Posterpräsentation
21. – 24. Febr. 2012	VAMDC Annual Meeting Mitglied des Local Organizing Committee
10. – 12. Mai, 2011	Workshop in „ <i>Pulsations of pre-main sequence stars and their impact on stellar evolution</i> “ Mitglied des Local Organizing Committee

Publikationen

Schmid, V. S., Themessl, N., Breger, M.,: „*Spectroscopic Frequencies of 4 CVn in 2010 and 2011*“, in Arbeit

Wien, am 03. Sept. 2012